

A network of cooler white dwarfs as infrared standards for flux calibration

Abigail K. Elms,^{1*} Nicola Pietro Gentile Fusillo,² Pier-Emmanuel Tremblay,¹ Ralph C. Bohlin,³ Mark A. Hollands,¹ Snehalata Sahu,¹ Mairi W. O’Brien,¹ Susana Deustua^{3,4} and Tim Cunningham⁵

¹Department of Physics, University of Warwick, Coventry, CV4 7AL, UK

²Department of Physics, Università degli Studi di Trieste, Via A. Valerio 2, 34127, Trieste, Italy

³Space Telescope Science Institute, 3700 San Martin Drive, Baltimore, MD 21218, USA

⁴Sensor Science Division, National Institute of Standards and Technology, Gaithersburg, MD 20899-8441, USA

⁵Center for Astrophysics | Harvard & Smithsonian, 60 Garden St., Cambridge, MA 02138, USA

Accepted XXX. Received YYY; in original form ZZZ

ABSTRACT

The accurate flux calibration of observational data is vital for astrophysics and cosmology because absolute flux uncertainties of stellar standards propagate into scientific results. With the ever higher precision achieved by telescopic missions (e.g. *JWST*) in the infrared (IR), suitable calibrators are required for this regime. The basis of the *Hubble Space Telescope* (*HST*) flux scale is defined by model fits of three hot ($T_{\text{eff}} > 30\,000$ K) hydrogen-atmosphere (DA) white dwarfs, which achieve an accuracy better than 1 per cent at optical wavelengths but falls below this level in the IR range. We present a network of 17 cooler DA white dwarfs with $T_{\text{eff}} < 20\,000$ K as spectrophotometric flux standards that are equally, if not more, accurate at IR wavelengths. Cooler white dwarfs do not suffer from non-local thermal equilibrium (NLTE) effects in continuum flux or from UV metal line blanketing, have a larger sky density, are generally closer to Earth with little or negligible interstellar reddening, and have energy distributions peaking in the optical or near-IR. Using the latest grid of DA LTE atmosphere models with three-dimensional (3D) convection, the observed Space Telescope Imaging Spectrometer (STIS) and Wide Field Camera three (WFC3) fluxes of our network are accurate to 3 per cent over most of the range 1450 – 16 000 Å, with a median standard deviation of 1.41 per cent. Fitting the *HST* STIS and WFC3 white dwarf SEDs and Balmer lines independently yields SEDs that agree within 3σ , which demonstrates the precision of the models for our network.

Key words: white dwarfs – standards – line: profiles – stars: fundamental parameters – infrared: general – methods: data analysis

1 INTRODUCTION

Now, more than ever, the creation and use of a reliable and self-consistent flux scale is of paramount importance. We have entered a pioneering era of space telescopes and instruments, which are providing previously unattainable data for objects in our Galaxy and beyond, especially in the near-IR (NIR; 0.8–5 μm) and mid-IR (MIR; 5 – 32 μm).

The *Hubble Space Telescope* (*HST*) provides high-resolution imaging and broad wavelength coverage from the far-ultraviolet (FUV; 0.0912 – 0.2 μm) to NIR. New generation observatories will compliment and further the scientific reach of *HST*, for instance the *James Webb Space Telescope* (*JWST*), *Euclid* spacecraft and *Nancy Grace Roman Space Telescope* (*RST*) have an array of high-resolution and high-sensitivity instruments which facilitate photometric and spectroscopic observations from the FUV to MIR regimes. Similar capabilities will be achieved with first generation high-resolution instrumentation on ground-based telescopes, such as the Multi-AO Imaging Camera for Deep Observations (MICADO) on the Extremely Large Telescope (ELT). Data from these instruments will revolutionise fields in cosmology, such as dark energy and dark mat-

ter, and astrophysics, such as stellar evolution and exoplanet studies. However, observational data calibration is a major source of uncertainty for many instruments and scientific fields (Hounsell et al. 2018; Tayar et al. 2022; Wilson et al. 2023). For example, the accurate comparison between the fluxes of distant redshifted and nearby supernovae (SNe) in the rest frame has a crucial impact on our understanding of the nature of the dark energy that is driving the observed accelerating cosmic expansion (Stubbs & Brown 2015; Scolnic et al. 2015, 2022; Brout et al. 2022). To reach this full scientific potential, photometric and spectroscopic instruments must be accurately calibrated on a single consistent flux scale, as uncertainties from flux standards propagate into scientific results (Hounsell et al. 2018).

To date, the most internally consistent set of primary flux standards are three hot ($T_{\text{eff}} > 30\,000$ K) hydrogen-atmosphere (DA) white dwarfs: GD 71, GD 153 and G191-B2B (Bohlin et al. 2014). The spectral energy distributions (SEDs), which are flux as a function of wavelength, of these primary standards provide the basis for calibration of the *HST* spectrophotometry, primarily from the Space Telescope Imaging Spectrometer (STIS), the Wide Field Camera three (WFC3) IR grisms, and the Near Infrared Camera and Multi-Object Spectrometer (NICMOS) (Bohlin 2014; Bohlin et al. 2020). While fits to Balmer lines determine T_{eff} and $\log g$, i.e. the shape of the SEDs, the absolute flux level is set by a reconciliation of the

* Contact e-mail: Abigail.Elms@warwick.ac.uk

original Vega flux at 5557.5 Å (vacuum; Megessier 1995) with the *Midcourse Space Experiment* (MSX) IR absolute flux to define the absolute flux at all wavelengths over the ultraviolet (UV), visible and NIR (Bohlin 2014; Bohlin et al. 2020). These SEDs provide the basis for the *HST* absolute flux scale and are publicly available on CALSPEC¹, which is a database of primary and secondary spectrophotometric absolute flux standard stars on the *HST* flux scale containing measured stellar spectra and modelled SEDs. CALSPEC standards are used for the calibration of *HST*, *JWST*, *Gaia* and other ground- and space-based instrumentation. Therefore, the precision and accuracy of observational astrophysical and cosmological studies which use CALSPEC standards are entirely dependent on the CALSPEC precision of measured and modelled SEDs.

Hot DA white dwarfs have fully radiative atmospheres, therefore, their optical spectra are relatively simple to model. Their effective temperature (T_{eff}) and surface gravity ($\log g$) determine accurate model SEDs (Holberg et al. 1985). SED models of the current three hot standards are consistent within 1 per cent at optical wavelengths (0.3 – 1 μm) with *HST* spectrophotometric observations (Bohlin 2014; Narayan et al. 2019). However, outside the optical, discrepancies of > 1 per cent are evident (Bohlin et al. 2011; Bohlin 2014; Bohlin et al. 2022), because uncertainties arise in hot white dwarf model atmospheres from complex non-local thermal equilibrium (NLTE) effects, trace metal contamination and UV metal line blanketing (Werner 1996; Gianninas et al. 2010; Rauch et al. 2013). Hot white dwarfs have a lower sky density ($\approx 0.75 \text{ deg}^{-2}$ at $G < 20$) than cooler white dwarfs, forcing the selection of more distant hot stars with larger reddening effects and more uncertain *Gaia* parallaxes. Also, hot white dwarf SEDs drop rapidly in flux at longer wavelengths. These sources of uncertainty are non-negligible and propagate into the results of scientific studies.

The need for faint standards, e.g. below the saturation limits of several instruments, has motivated the expansion of hot white dwarf standards in recent years using *HST* spectrophotometry from faint ($16.5 < V < 19.5$) and photometrically stable DA white dwarfs spanning the whole sky (Narayan et al. 2016, 2019; Calamida et al. 2022; Axelrod et al. 2023). These studies have achieved consistency within 1 per cent of the *HST* flux scale at optical wavelengths, thus establishing all-sky spectrophotometric secondary standards for wide-field optical surveys. Good agreement was also found in the NIR regime with WFC3 observations.

We propose to add a network of 17 cooler DA white dwarfs with $T_{\text{eff}} < 20\,000 \text{ K}$ as secondary spectrophotometric flux standards on the *HST* flux scale. Our network has *HST*/STIS flux calibrated spectra, with 16/17 supplemented by *HST*/WFC3 spectrophotometry, thus they are tied to the three CALSPEC primary standards. Cooler white dwarfs than the current primary hot standards have been proposed in recent years to have a comparable, or even higher, accuracy at IR wavelengths compared to hot white dwarfs (Tremblay et al. 2017; Gentile Fusillo et al. 2020). DA white dwarfs with $T_{\text{eff}} < 20\,000 \text{ K}$ suffer much less from NLTE effects or UV metal line blanketing, have a larger sky density than hot white dwarfs, their energy distributions peak in the optical/NIR, and are still relatively bright in the IR compared to their hotter counterparts. Cooler white dwarfs at distances $\leq 100 \text{ pc}$ have the advantage of having less reddening than further away hot white dwarfs, while still being reliable calibrators for IR observing modes. The latest DA model atmospheres can effectively account for convective effects which are important for white dwarfs

with $T_{\text{eff}} \leq 13\,000 \text{ K}$ (Tremblay et al. 2013, 2019) so there are no reservations about modelling cooler white dwarfs which might have arisen decades ago, even though dense atmospheres below 6000 K are still subject to a low-mass problem (O’Brien et al. 2024).

The exclusive use of hot white dwarfs as flux calibrators may not be the optimal choice for achieving the highest accuracy possible, in particular with the dawn of next-generation IR missions. Our proposed network of 17 cooler calibrators can be used in parallel with hot white dwarf calibrators depending on the science case. This network will provide an independent estimate for secondary SEDs compared to the current primary SEDs; and the difference between SEDs based on cool or hot white dwarfs sets limits on the precision of flux calibrations. We split our network into 13 warm ($13\,000 \text{ K} < T_{\text{eff}} < 20\,000 \text{ K}$) flux standard candidates and four extra flux standard candidates, which consist of the three coolest ($T_{\text{eff}} < 13\,000 \text{ K}$) white dwarfs in the network and one which has no *HST*/WFC3 spectrophotometry. There is an on-sky separation of < 4 h between the white dwarfs across the whole sky, which ensures adequate sky coverage for the vast majority of science cases.

Section 2 presents *HST* spectrophotometric observations of the 17 white dwarfs in our network, in addition to their *Gaia* Data Release 3 (DR3) astrometry and optical and IR photometry. We describe the fitting procedures implemented on the observed *HST* data with our model atmospheres in Section 3 which allow us to derive two sets of independent T_{eff} and $\log g$ best-fitting parameters, in addition to synthetic photometry and *Gaia* atmospheric parameters. In Section 4 we discuss our results and conclude in Section 5.

2 OBSERVATIONS

2.1 Hubble Space Telescope spectrophotometry

Our network of 17 flux standard candidates was built using spectrophotometric observations from three *HST* programmes that made use of the STIS and WFC3 instruments. WD 1327–083 and WD 2341+322 were observed in a Cycle 23 (GP-14213) pilot programme on using cooler white dwarfs than the current hot primary standards as near-IR and IR flux calibrators. WD 0352+096 has been observed intermittently over the past few decades, with the latest observations being from a Cycle 25 (GP-15485) programme for CALSPEC and *JWST* standard stars. The remaining 14 white dwarfs were observed in a Cycle 28 (GP-16249) programme specifically targeting candidates for our flux standard network. All 17 stars were selected because they do not have unresolved stellar companions in *HST* and *Gaia*, have hydrogen-dominated atmospheres (spectral type DA), have $T_{\text{eff}} < 20\,000 \text{ K}$, and no observed photometric or spectroscopic variability due to pulsations or magnetic phenomena - see Section 4.4 for flags from the literature on variability, metal traces, observed magnetism and binarity for the individual white dwarfs in our network.

The STIS low dispersion (L) spectra were obtained with a $52'' \times 2.0''$ long slit on the G140L, G230L, G430L and G750L gratings which cover 1140 – 10 200 Å and the WFC3 spectra were obtained with the G102 and G141 grisms which cover 8000 – 17 000 Å. STIS and WFC3 spectrophotometry were merged at 10 115 Å to form complete *HST* SEDs spanning 1140 – 17 000 Å for all 17 candidates except WD 0352+096 which does not have WFC3 data. A log of the *HST* spectrophotometric observations are given in Table A1.

¹ <https://www.stsci.edu/hst/instrumentation/reference-data-for-calibration-and-tools/astronomical-catalogs/calspec>

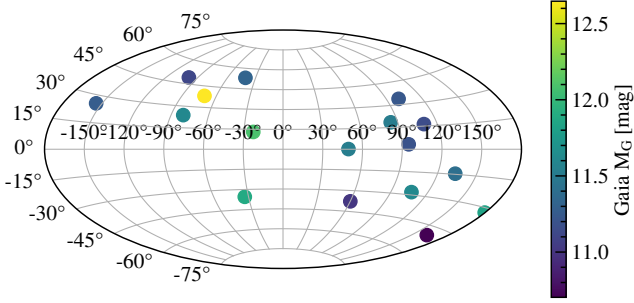


Figure 1. Galactic coordinates (latitude and longitude in the J2016.0 epoch) of the 17 white dwarf flux standard candidates from *Gaia* DR3, with their colour representing their absolute magnitudes, M_G , computed using the *Gaia* G magnitude and the *Gaia* parallax (Table 1).

2.2 *Gaia* DR3 astrometry

The *Gaia* DR3 astrometry for the 17 DA white dwarfs proposed as flux standards is displayed in Table 1 and the spatial distribution in Galactic coordinates of the network is shown in Fig. 1. The stars are all within 40 pc and have absolute *Gaia* G magnitudes (M_G) of < 12.7 mag so they are relatively bright compared to white dwarfs in the same volume, which peak at absolute magnitudes of approximately 14.5 mag (O’Brien et al. 2024).

Data for two of the current hot primary standard white dwarfs, GD 153 and GD 71, are also given in Table 1 for comparison to the 17 flux standard candidates. The third hot primary standard, G191-B2B, is not included in this paper (see Section 3.1 for more details).

2.3 Photometry

Most white dwarfs in our network have optical photometry from *Gaia* DR3 G , G_{BP} and G_{RP} bands (Gaia Collaboration et al. 2023), in addition to IR photometry from the Two Micron All Sky Survey J , H and K_S bands (2MASS; Skrutskie et al. 2006) and the Wide-field Infrared Survey Explorer (WISE; Wright et al. 2010) $W1$ and $W2$ bands from the AllWISE source catalogue. Observed photometry is displayed in Table 4.

3 ANALYSIS

3.1 Spectrophotometric fitting

The latest (March 2024) grid of 3D pure-hydrogen (DA) local thermal equilibrium (LTE) atmosphere models were used to fit the *HST* spectrophotometry of the 17 DA white dwarfs proposed as flux standards. The grid is an updated version of the work in Tremblay et al. (2013) and Tremblay et al. (2015a), which now has an extended resolution and wavelength coverage (40 – 600 000 Å), is in vacuum wavelengths, and can be used with or without H_2 molecular lines in the UV. This work does not use high-resolution UV data so we employ the grid without H_2 molecular lines. The grid includes models for $7.0 \leq \log g \leq 9.0$ in steps of 0.5 dex (cgs units) and $1500 \leq T_{\text{eff}} \leq 40\,000$ K. We have used LTE models because NLTE effects at $< 40\,000$ K are only noticeable on the central, high spectral resolution cores of Balmer lines (Napiwotzki et al. 2020; Munday et al. 2024), which is inconsequential for continuum flux calibration. At $T_{\text{eff}} \leq 13\,000$ K atmospheric convection becomes important to predict continuum fluxes from UV to IR, hence we use 3D models

which have no free parameters unlike the previous 1D grids based on the mixing-length theory of convection (Tremblay et al. 2013).

Ideally, atmospheric models should correctly predict the SED flux and Balmer line profiles of white dwarf flux standards independently to sub-percent precision. Therefore, we fit the network in two different ways: 1) SED fit of the continuum and *Gaia* DR3 parallax, omitting the Balmer line regions; 2) Balmer line fit of $H\beta - H\gamma$. This method allows us to determine two independent T_{eff} and $\log g$ values for each star, thus defining model absolute fluxes with the help of a mass-radius ($M-R$) relation (see e.g. Bédard et al. 2020).

The same fitting methods were conducted on the current hot standards GD 153 and GD 71, except that we used a 1D DA NLTE grid of models due to these stars having $T_{\text{eff}} \approx 40\,000$ K and being outside of the range of convection (Tremblay et al. 2011). This grid is in air wavelengths and ranges from $6.5 \leq \log g \leq 9.5$ in steps of 0.5 dex and $1500 \leq T_{\text{eff}} \leq 140\,000$ K. We did not include the current hot standard G191-B2B in our analysis because it has trace metals that strongly influence NLTE effects, thus a different model grid would have to be used to accurately fit its SED (Gianninas et al. 2010; Bohlin et al. 2020).

The input physics prescription and numerical methods for both DA 3D LTE and 1D NLTE model grids can be found on P.-E. Tremblay’s Source Model Data webpage².

3.1.1 STIS and WFC3 SED fitting

Each observed STIS and WFC3 *HST* spectra were fit with model atmospheres by minimising the reduced χ^2 using the *scipy* optimize trust region reflective (trf) algorithm, which is a non-linear least-squares method (Byrd et al. 1987). The fits neglect regions bluer than 1450 Å to avoid the broad Lyman- α H_2^+ satellite region at 1380 – 1410 Å, which appears for stars $T_{\text{eff}} < 20\,000$ K (Koester et al. 1985) and increases in strength (i.e. extends to redder wavelengths) for decreasing temperatures - thus, the fits were started at 1700 Å for the two coolest stars in the network WD 1202–232 and WD 1544–377. WD 2341+322 is the third coolest star in the network and has a Lyman- α satellite from H-H collisions at ≈ 1600 Å, however our models fit this feature well and has been proven to be a good indicator of atmospheric parameters (Xu et al. 2013; Greenstein & Oke 1979; Wegner 1982; Koester et al. 1985; Nelan & Wegner 1985) so we kept it in the fit by starting at 1450 Å like the warmer objects in the network. The reddest WFC3 grism extends to 17 000 Å so to avoid the end of the grism where measurements can get unreliable we neglected all wavelengths redder than 16 000 Å, except WD 0352+096 which does not have WFC3 data so we end the fit at 10 000 Å to avoid the edge of the STIS G750L grating (at 10 238 Å). The Balmer line regions 3815 – 4490 Å, 4681 – 5041 Å and 6385 – 6745 Å were masked in all fits to ensure independent atmospheric parameters were obtained to the separate Balmer line fit parameters.

The DA model Eddington fluxes, H_ν , were converted to $H_\lambda(\lambda)$ for the fits, then compared to the observed fluxes, $f_\lambda(\lambda)$, using

$$f_\lambda(\lambda) = 4\pi \left(\frac{R}{D} \right)^2 H_\lambda(\lambda), \quad (1)$$

where R is the white dwarf radius and D is the distance to the white dwarf from Earth, constrained from the *Gaia* DR3 parallax. The model fluxes were reddened (extinguished) using the G23 model

² <https://warwick.ac.uk/fac/sci/physics/research/astro/people/tremblay/modelgrids/>

Table 1. *Gaia* DR3 astrometry for the 17 DA white dwarfs proposed as flux standards. Proper motions, μ , are given in the right ascension (α) and declination (δ) directions. Absolute magnitudes, M_G , are computed using the *Gaia* *G* magnitude and the *Gaia* parallax. Values are given in the J2016.0 epoch.

Object	<i>Gaia</i> DR3 Designation	RA [deg]	Dec [deg]	$\mu_\alpha \cos(\delta)$ [mas yr ⁻¹]	μ_δ [mas yr ⁻¹]	Parallax [mas]	Distance [pc]	M_G [mag]
Hot primary standards								
GD 153	3944400490365194368	194.259	22.030	-38.402 ± 0.045	-202.990 ± 0.051	14.593 ± 0.038	68.526 ± 0.177	9.132 ± 0.003
GD 71	3348071631670500736	88.115	15.886	76.728 ± 0.053	-172.960 ± 0.038	19.564 ± 0.055	51.115 ± 0.144	9.457 ± 0.003
Warm flux standard candidates								
WD 0148+467	356922880493142016	28.012	47.002	4.645 ± 0.031	122.025 ± 0.027	60.564 ± 0.031	16.511 ± 0.008	11.407 ± 0.003
WD 0227+050	2516322146457318144	37.570	5.264	76.958 ± 0.049	-24.502 ± 0.039	37.711 ± 0.051	26.517 ± 0.036	10.703 ± 0.003
WD 0809+177	657056745624156416	123.158	17.617	73.482 ± 0.026	-87.171 ± 0.020	36.977 ± 0.025	27.044 ± 0.018	11.269 ± 0.003
WD 1105-340	5401688425816913920	166.950	-34.349	39.894 ± 0.021	-263.429 ± 0.019	38.195 ± 0.021	26.181 ± 0.014	11.610 ± 0.003
WD 1105-048	3788194488314248832	167.000	-5.160	-55.547 ± 0.031	-442.634 ± 0.028	40.293 ± 0.032	24.818 ± 0.020	11.117 ± 0.003
WD 1327-083	3630035787972473600	202.552	-8.577	-1111.205 ± 0.048	-472.540 ± 0.028	62.148 ± 0.044	16.091 ± 0.011	11.322 ± 0.003
WD 1713+695	1638563322306634368	258.275	69.522	-55.513 ± 0.020	-343.042 ± 0.025	38.094 ± 0.018	26.251 ± 0.012	11.232 ± 0.003
WD 1911+536	2140481412496465152	288.203	53.721	144.450 ± 0.022	136.061 ± 0.019	45.109 ± 0.018	22.169 ± 0.009	11.518 ± 0.003
WD 1919+145	4319908862597055232	290.418	14.678	-33.016 ± 0.027	-75.933 ± 0.023	50.308 ± 0.030	19.878 ± 0.012	11.527 ± 0.003
WD 2039-682	6424566979354709248	311.092	-68.090	182.095 ± 0.018	-228.167 ± 0.023	51.099 ± 0.025	19.570 ± 0.010	11.882 ± 0.003
WD 2117+539	2176116580055936512	319.734	54.212	-85.450 ± 0.026	193.193 ± 0.026	57.764 ± 0.022	17.312 ± 0.006	11.201 ± 0.003
WD 2126+734	2274076297221555968	321.741	73.644	55.338 ± 0.030	-314.200 ± 0.030	44.992 ± 0.026	22.226 ± 0.013	11.153 ± 0.003
WD 2149+021	2693940725141960192	328.106	2.387	15.323 ± 0.042	-300.533 ± 0.044	44.326 ± 0.043	22.560 ± 0.022	11.010 ± 0.003
Extra flux standard candidates								
WD 0352+096	3302846072717868416	58.842	9.788	173.274 ± 0.035	-5.569 ± 0.025	28.587 ± 0.037	34.981 ± 0.045	11.829 ± 0.003
WD 1202-232	3489719481290397696	181.361	-23.552	41.819 ± 0.021	226.558 ± 0.020	95.902 ± 0.018	10.427 ± 0.002	12.647 ± 0.003
WD 1544-377	6009537829925128064	236.873	-37.920	-423.692 ± 0.031	-209.108 ± 0.025	65.689 ± 0.026	15.223 ± 0.006	12.088 ± 0.003
WD 2341+322	2871730307948650368	355.960	32.546	-215.905 ± 0.033	-59.871 ± 0.021	53.762 ± 0.027	18.601 ± 0.009	11.619 ± 0.003

from [Gordon et al. \(2023\)](#), which is the latest extinction curve in the python package `dust_extinction3` for 912 Å to 32 μm and $R(V) = A(V)/E(B - V)$. We used $R(V) = 3.1$ as this is the often used Milky Way average value ([Johnson 1965](#); [Schultz & Wiemer 1975](#); [Whittet & van Breda 1980](#); [Fitzpatrick & Massa 1999](#)). The T_{eff} , $\log g$, parallax and $E(B - V)$ were free parameters in the fits. The bounds for T_{eff} and $\log g$ were determined by the model grid limits, parallax was bounded by $\pm 3\sigma$ of the *Gaia* DR3 parallax errors, and $E(B - V)$ had arbitrary bounds of 0.00 – 0.05 mag due to all white dwarfs in the network being < 40 pc thus having minimal reddening effects. We used the DA M - R relation with thick hydrogen layers and carbon-oxygen cores from [Bédard et al. \(2020\)⁴](#) to determine R (and white dwarf mass) using the best-fitting T_{eff} , $\log g$ and parallax.

Statistical uncertainties were computed from the covariance matrix of the model atmosphere fit scaled by reduced χ^2 to account for the goodness of fit. The systematic error on SED fits were computed by fitting the UV (1450 – 3065 Å) and combined optical+NIR (3065 – 16 000 Å) regions separately to obtain two sets of T_{eff} and $\log g$ best-fitting parameters.

These pairs of T_{eff} and $\log g$ disagreed by far more than the statistical errors, indicating some unmodelled systematic uncertainty. To quantify these, we assumed that each white dwarf required some additional variance in $\ln T_{\text{eff}}$ and $\log g$ that is the same for all objects. We then sought to determine these systematic uncertainties via a maximum-likelihood approach. For a quantity x (where x is either $\ln T_{\text{eff}}$ or $\log g$) observed for a single system N times (in our case $N = 2$), the i th observation, x_i , can be considered to be drawn from a normal distribution with unknown mean μ and variance σ^2 , with additional measurement uncertainty, e_i . The likelihood of all N observations is therefore

$$L(\mathbf{x}|\mu, \sigma, \mathbf{e}) = \prod_i^N \frac{1}{\sqrt{2\pi v_i}} \exp\left(-\frac{(x_i - \mu)^2}{2v_i}\right), \quad (2)$$

where $v_i = \sigma^2 + e_i^2$. Since we are not specifically interested in μ , only σ , we can integrate over μ , reducing the dimensionality to a marginal likelihood that depends only σ . This integral has an analytic solution which can be written as

$$\ln L(\mathbf{x}|\sigma, \mathbf{e}) = k - \frac{1}{2} \left(\ln a - b^2/a + c + d \right), \quad (3)$$

where k is a normalising constant, and a – d are sums over the observations given by

$$a = \sum_i^N \frac{1}{v_i}, \quad b = \sum_i^N \frac{x_i}{v_i}, \quad c = \sum_i^N \frac{x_i^2}{v_i}, \quad d = \sum_i^N \ln v_i, \quad (4)$$

and are themselves functions of σ . Finally, for M systems with index j , the log-likelihood (dropping proportionality constants)

$$\ln L(\mathbf{x}_1, \dots, \mathbf{x}_M | \sigma, \mathbf{e}_1, \dots, \mathbf{e}_M) = \sum_j^M \ln L(\mathbf{x}_j | \sigma, \mathbf{e}_j). \quad (5)$$

Because of the marginalisation step, the final likelihood depends only on σ . Therefore determining the maximum-likelihood is a simple case of plotting as a function of σ and visually determining the location of the maximum to whatever precision is desired.

For our 13 warm flux standard candidate white dwarfs, each with two observations, we determined systematic uncertainties of 1.1 per cent in T_{eff} (i.e. 0.011 in $\ln T_{\text{eff}}$), and 0.01 dex in $\log g$. Data from the extra flux standard candidates is not included in the systematic uncertainty determination due to their SED fits spanning different wavelength ranges to the other 13 candidates. We apply the systematic uncertainties in T_{eff} and $\log g$ to all 17 flux standard candidates and the two primary standards. The combined statistical and systematic uncertainties are displayed in Table 2 with the best-fitting T_{eff} and $\log g$ parameters for our network and the two primary standards. The best-fitting extinction value is also quoted in Table 2 from each SED fit to three decimal places.

The SED fits between the observed spectrophotometry and best-fitting models for the 13 warm and four extra flux standard candidates are shown in the top left panels of Figures 2 (continued in Figure B1) and 3, respectively. The SED flux residuals are shown

³ https://github.com/karllark/dust_extinction

⁴ <https://www.astro.umontreal.ca/~bergeron/CoolingModels/>

in the bottom left panels of the same figures. The best-fitting SED models for the flux standard candidates include the parameters T_{eff} , $\log g$, $E(B - V)$, radius and mass. The best-fitting SED models and parameters are available with the electronic distribution of this paper and on CALSPEC, except the models for WD 1202–232 and WD 1544–377 which are not included in CALSPEC due to potential modelling issues and/or contamination in the IR (see Section 4.1). The models for WD 1202–232 and WD 1544–377 included in the electronic distribution of this paper are cropped at 2300 – 12 700 Å and 2400 – 12 500 Å, respectively, as the flux residuals are majoritively within 5 per cent in these regions.

We calculated the standard deviation of the flux residuals for all 17 candidates and the two hot primary standards over the entire wavelength range of each SED fit, in addition to the UV and combined optical+NIR ranges. The percentages are given in Table 3.

3.1.2 Balmer line fitting

For each of our 17 flux standard candidates, an independent set of T_{eff} and $\log g$ values can be obtained by directly comparing the Balmer line profiles with our sets of models. We do this by first continuum normalising both the models and the STIS spectra by fitting a spline, and then cropping out each Balmer line (e.g. Figure 2 right panels). We then fit the cropped $H\beta$ to $H\eta$ absorption features with our DA model atmospheres using the same `scipy optimize trf` reduced χ^2 minimisation technique as our SED fits. T_{eff} , $\log g$ and radial velocity were free parameters in the fits. The bounds for T_{eff} and $\log g$ were determined by the model grid limits, whereas radial velocity was bounded by the range $-300 - 300 \text{ km s}^{-1}$. The same DA M - R relation as in our SED fits (Section 3.1.1) was used to determine R (and white dwarf mass) using the best-fitting T_{eff} and $\log g$. The $H\eta$ Balmer line was excluded from the fits for GD 153 and GD 71 because it has negligible equivalent width for these hot stars.

Unlike the SED fits, for Balmer line modelling the arbitrarily high natural resolution of our DA models needs to be degraded to match that of STIS. This can be achieved by convolving the models with the appropriate STIS grating Line Spread Function (LSF) at the slit width matching that of our observations. Tabulated LSFs are available at the *HST* STIS web pages⁵, which specifies the shape of a monochromatic line feature as observed with the specified instrumental resolution and provides an empirical description of the light distribution along the primary dispersion axis. $H\beta$ to $H\eta$ are covered by the G430L grating and $H\alpha$ is covered by the G750L grating. In our analysis we opt to exclude $H\alpha$ allowing us to use only the G430L tables with no need to splice together models at different resolutions. The Rel Pixel column shows the exact relative spacing of the grating in pixels, this is multiplied by the the appropriate grating pixel dispersion in order to obtain the spacing in Angstroms. The G430L grating is split between 3200 Å and 5500 Å LSF tables therefore we averaged them to give a full coverage overview.

Convolving our models directly with the LSF proved computationally expensive and not feasible for use on large numbers of stars. Furthermore, severe edge effects arise at the end points of the LSF grid resulting in warping of the model spectra. We instead decided to fit the LSF tabulated data and create a function which closely reproduces the relative pixel spacing values of the grating. We used the sum of three Gaussian profiles and produced a function which matches the actual LSF data to within 1 per cent. This custom LSF

function was then used in the convolution to degrade our models to the resolution of the STIS G430L grating.

The Balmer line best-fitting model to the observed spectrophotometry for the 13 warm and four extra flux standard candidates are shown in the right panels of Figures 2 (continued in Figure B1) and 3, respectively. The best-fitting T_{eff} and $\log g$ are displayed in Table 2. The uncertainties of the fit parameters are dependent on one another and are computed from the covariance matrix of the model atmosphere fit scaled by reduced χ^2 to account for the goodness of fit, therefore they are statistical in nature and do not account for systematic uncertainty.

3.2 Synthetic magnitudes and photometric fitting

Synthetic magnitudes were computed for the *Gaia* DR3 G , G_{BP} and G_{RP} bands, 2MASS J , H and K_S bands, and WISE $W1$ and $W2$ bands using our best-fitting STIS and WFC3 T_{eff} and $\log g$ parameters for the 17 flux standard candidates, in addition to GD 153 and GD 71 (Table 2). Synthetic apparent magnitudes, m , for *Gaia* DR3 photometry were computed by integrating under the model curves for each filter bandpass using

$$m = -2.5 \log \left(\frac{\int T(\lambda) f_{\lambda}(\lambda, T_{\text{eff}}, \log g) \lambda d\lambda}{\int T(\lambda) \lambda d\lambda} \right) + c, \quad (6)$$

where λ is the wavelength, $T(\lambda)$ is the filter transmission function for any *Gaia* DR3 filter, obtained from the Spanish Virtual Observatory (SVO) Filter Profile Service (Rodrigo et al. 2012), $f_{\lambda}(\lambda, T_{\text{eff}}, \log g)$ is the model flux at the distance of the white dwarf from Equation 1, and c is the zeropoint magnitude for the given filter.

For 2MASS and WISE, synthetic magnitudes were computed using

$$m = -2.5 \log \left(\frac{\int T(\lambda) f_{\lambda}(\lambda, T_{\text{eff}}, \log g) d\lambda}{\int T(\lambda) d\lambda} \right) + c, \quad (7)$$

where filter transmission functions were also obtained from SVO.

All synthetic and observed magnitudes are in the Vega magnitude system and are displayed in Table 4. The Vega SEDs from CALSPEC used for synthetic magnitudes were a modified version of `alpha_lyr_mod_002.fits`⁶ in the UV and optical range (to $\approx 1 \mu\text{m}$, i.e. *Gaia* filters; Busso et al. 2022) and `alpha_lyr_stis_011.fits` beyond $1 \mu\text{m}$ (i.e. 2MASS and WISE filters).

We corrected the synthetic magnitudes for reddening by evaluating the extinction A_{λ} using the G23 model (Gordon et al. 2023) at the effective wavelengths of each filter obtained from SVO. We used $R(V) = 3.1$ and the best-fitting $E(B - V)$ values from our SED fits in Section 3.1.1 given in Table 2.

In the NASA/IPAC (Infrared Processing and Analysis Center) Infrared Science Archive, WD 2117+539 has no observed WISE data and WD 1544–377 has no observed 2MASS nor WISE data. WD 1919+145 has no observed 2MASS J magnitude error meaning the reported J magnitude is a 95 per cent confidence upper limit, thus we exclude it from this work.

The magnitude difference between observed and synthetic photometry for our network are shown in each band for *Gaia*, 2MASS and WISE in Figures 4, 5 and 6, respectively, for those stars with observed photometry. WD 1327–083, WD 1919+145 and WD 2126+734 are

⁵ <https://www.stsci.edu/hst/instrumentation/stis/performance/spectral-resolution>

⁶ https://gea.esac.esa.int/archive/documentation/GDR3/Data_processing/chap_cu5pho/cu5pho_sec_photProc/cu5pho_ssec_photCal.html#SSS3.P2

Table 2. Atmospheric parameters of the 17 DA white dwarfs proposed as flux standards from two fitting methods: 1) SED fit of the continuum and *Gaia* DR3 parallax, omitting the Balmer regions; 2) Balmer line fit of $H\beta - H\gamma$. The uncertainties on the SED fits correspond to 1σ and are a combination of the statistical errors from the fits and the systematic errors (1.1 per cent in T_{eff} and 0.01 dex in $\log g$) obtained in Section 3.1.1. The quoted uncertainties on the Balmer line fits correspond to 1σ and are purely of statistical nature as derived from the fits. These Balmer line fit uncertainties are found to be underestimated in Section 4.2 hence we recommend the reader to apply a scale factor of $\times 3$ for further analysis. $\sigma_{T_{\text{eff}}}$ and $\sigma_{\log g}$ correspond to how many σ apart the best-fitting T_{eff} and $\log g$ parameters are from the SED and Balmer line fits. $E(B - V)$ values which are quoted as 0.000 may be non-zero (< 0.0005 mag) in the fit and analysis.

Object	SED fit		Balmer line fit		$E(B - V)$ ($R_V = 3.1$) [mag]	$\sigma_{T_{\text{eff}}}$	$\sigma_{\log g}$
	T_{eff} [K]	$\log g$ [dex]	T_{eff} [K]	$\log g$ [dex]			
Hot primary standards							
GD 153	40120 ± 443	7.818 ± 0.021	39240 ± 251	7.750 ± 0.026	0.000	1.007	0.843
GD 71	33379 ± 367	7.822 ± 0.017	33054 ± 107	7.780 ± 0.020	0.000	0.666	0.673
Warm flux standard candidates							
WD 0148+467	14483 ± 160	8.025 ± 0.012	13784 ± 81	8.032 ± 0.014	0.000	2.403	0.182
WD 0227+050	19190 ± 213	7.903 ± 0.017	19093 ± 55	7.894 ± 0.013	0.000	0.362	0.200
WD 0809+177	16371 ± 181	8.078 ± 0.015	16152 ± 73	8.102 ± 0.015	0.000	0.767	0.509
WD 1105-340	14099 ± 156	8.102 ± 0.014	13618 ± 190	8.120 ± 0.029	0.000	0.815	0.198
WD 1105-048	15826 ± 175	7.940 ± 0.015	15602 ± 74	7.949 ± 0.014	0.000	2.795	0.199
WD 1327-083	15100 ± 167	8.007 ± 0.015	14368 ± 103	7.984 ± 0.019	0.004	2.091	0.356
WD 1713+695	16063 ± 178	8.026 ± 0.015	15629 ± 71	7.979 ± 0.014	0.000	1.563	1.072
WD 1911+536	17424 ± 192	8.316 ± 0.016	17198 ± 71	8.335 ± 0.012	0.000	0.784	0.481
WD 1919+145	15364 ± 171	8.174 ± 0.017	14750 ± 67	8.173 ± 0.015	0.000	2.335	0.003
WD 2039-682	17076 ± 188	8.497 ± 0.016	16726 ± 76	8.502 ± 0.016	0.002	1.182	0.088
WD 2117+539	15583 ± 172	7.949 ± 0.016	14541 ± 72	7.921 ± 0.013	0.002	3.768	0.647
WD 2126+734	16050 ± 177	7.967 ± 0.015	15535 ± 65	7.967 ± 0.013	0.003	1.953	0.005
WD 2149+021	17692 ± 196	8.009 ± 0.016	17695 ± 72	8.019 ± 0.015	0.000	0.011	0.221
Extra flux standard candidates							
WD 0352+096	14810 ± 164	8.320 ± 0.015	14000 ± 260	8.341 ± 0.023	0.000	1.017	0.308
WD 1202-232	8854 ± 100	8.024 ± 0.023	8736 ± 21	7.980 ± 0.019	0.008	0.999	0.716
WD 1544-377	10303 ± 121	7.999 ± 0.033	10581 ± 46	8.012 ± 0.025	0.003	1.517	0.154
WD 2341+322	12852 ± 142	8.027 ± 0.013	12775 ± 128	8.036 ± 0.021	0.000	0.190	0.143

Table 3. The standard deviation flux residual across three different wavelength ranges of the SED fit: the entire wavelength range of each SED fit; the UV region; the optical+NIR region. Quantities are given as a percentage.

Object	Entire wavelength range per cent	UV per cent	optical+NIR per cent
Hot primary standards			
GD 153	0.36	0.31	0.36
GD 71	0.33	0.30	0.35
Warm flux standard candidates			
WD 0148+467	1.24	1.30	1.04
WD 0227+050	1.12	1.17	0.99
WD 0809+177	1.43	1.58	1.26
WD 1105-340	2.58	2.68	1.59
WD 1105-048	1.31	1.50	1.12
WD 1327-083	1.49	1.43	1.19
WD 1713+695	1.41	1.56	1.21
WD 1911+536	1.31	1.35	1.18
WD 1919+145	1.38	1.63	1.10
WD 2039-682	1.33	1.47	1.15
WD 2117+539	1.49	1.33	0.91
WD 2126+734	1.23	1.30	0.98
WD 2149+021	1.34	1.23	1.01
Extra flux standard candidates			
WD 0352+096	2.08	2.22	1.52
WD 1202-232	4.61	2.34	0.96
WD 1544-377	4.42	1.27	2.44
WD 2341+322	1.89	2.19	1.28

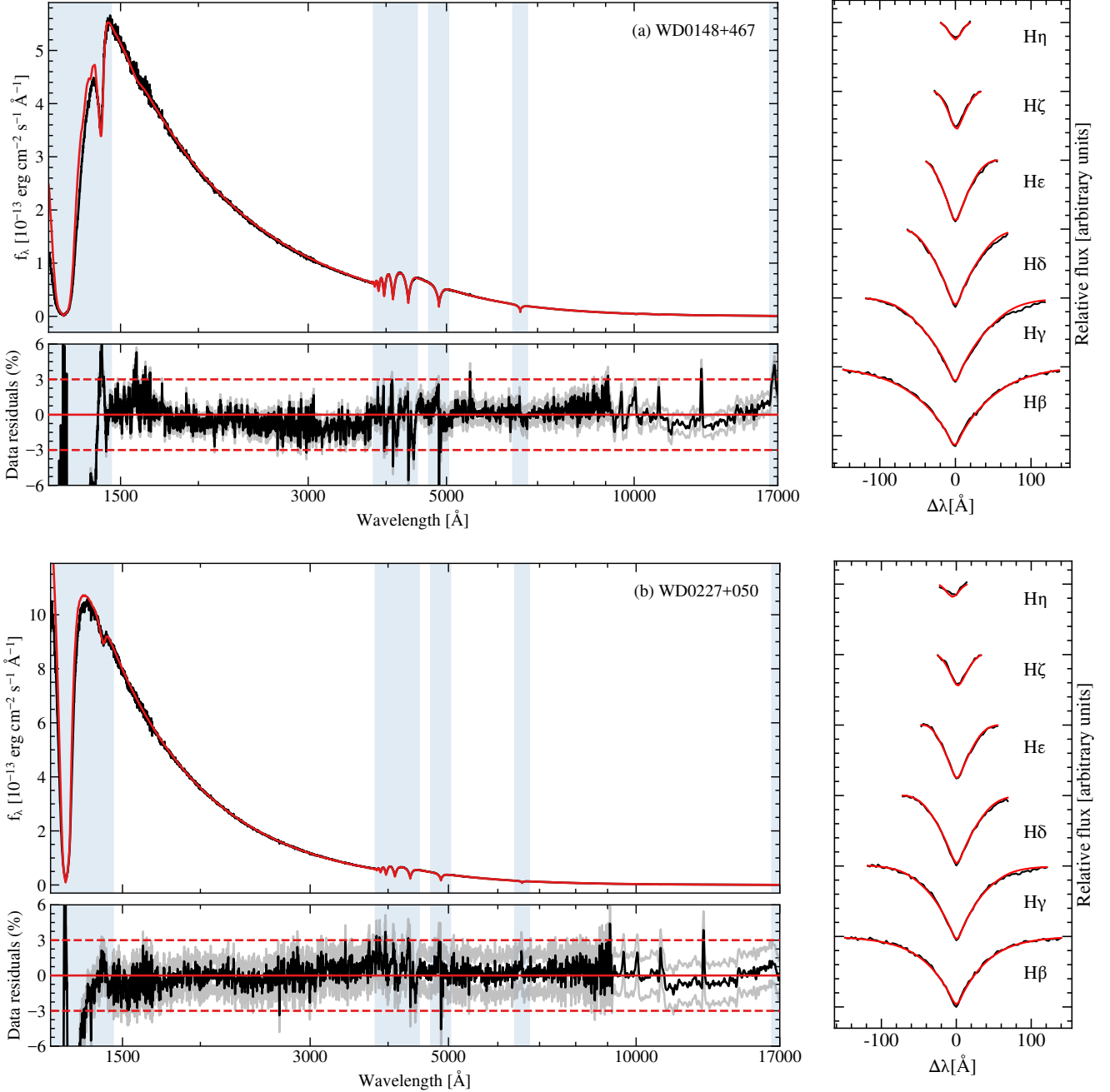


Figure 2. Spectrophotometric fits of the STIS and WFC3 data for two of the 13 warm white dwarfs proposed as flux standard candidates, with the WD name of each star given in the corner of the top left panels. The spectrophotometric fits of the remaining 11 warm white dwarfs are in Figures B1. *Top left:* SED fit between the observed spectrophotometry (black) and best-fitting model (red). *Bottom left:* Flux residuals from the corresponding SED fit, where the black line is the calculated residual, grey lines indicate residuals $\pm 1\sigma$ using only the statistical errors from the fits, and red lines show residuals of 0 and ± 3 per cent as a guide. The shaded blue regions in the left panels indicate wavelength ranges excluded from the fits. *Right:* Balmer line fits for $H\beta$ to $H\eta$ between the observed spectrophotometry (black) and best-fitting model (red). The line profiles are vertically offset for clarity. The best-fitting parameters for the SED and Balmer line fits are found in Table 2.

not included in Figure 6 because their observed and synthetic photometries are $> 3\sigma$ discrepant (see Section 4.3). The error bars in Figures 4 - 6 represent the combined observed and synthetic magnitude errors, where synthetic errors were calculated from the minimum statistical T_{eff} and $\log g$ errors on our STIS and WFC3 SED fits (Table 2).

Finally, we photometrically fit the observed *Gaia* DR3 G , G_{BP}

and G_{RP} band photometry for our network and the two hot standards using Equation 6 and the same DA model grids as in our SED and Balmer line fitting to obtain *Gaia* atmospheric parameters. Table 5 displays the best-fitting T_{eff} and $\log g$ parameters obtained from our photometric fits. The differences between *Gaia* photometric fit parameters and those obtained from our *HST* STIS and WFC3 SED fits are shown in Table 5 as $\sigma_{T_{\text{eff}}}$ and $\sigma_{\log g}$.

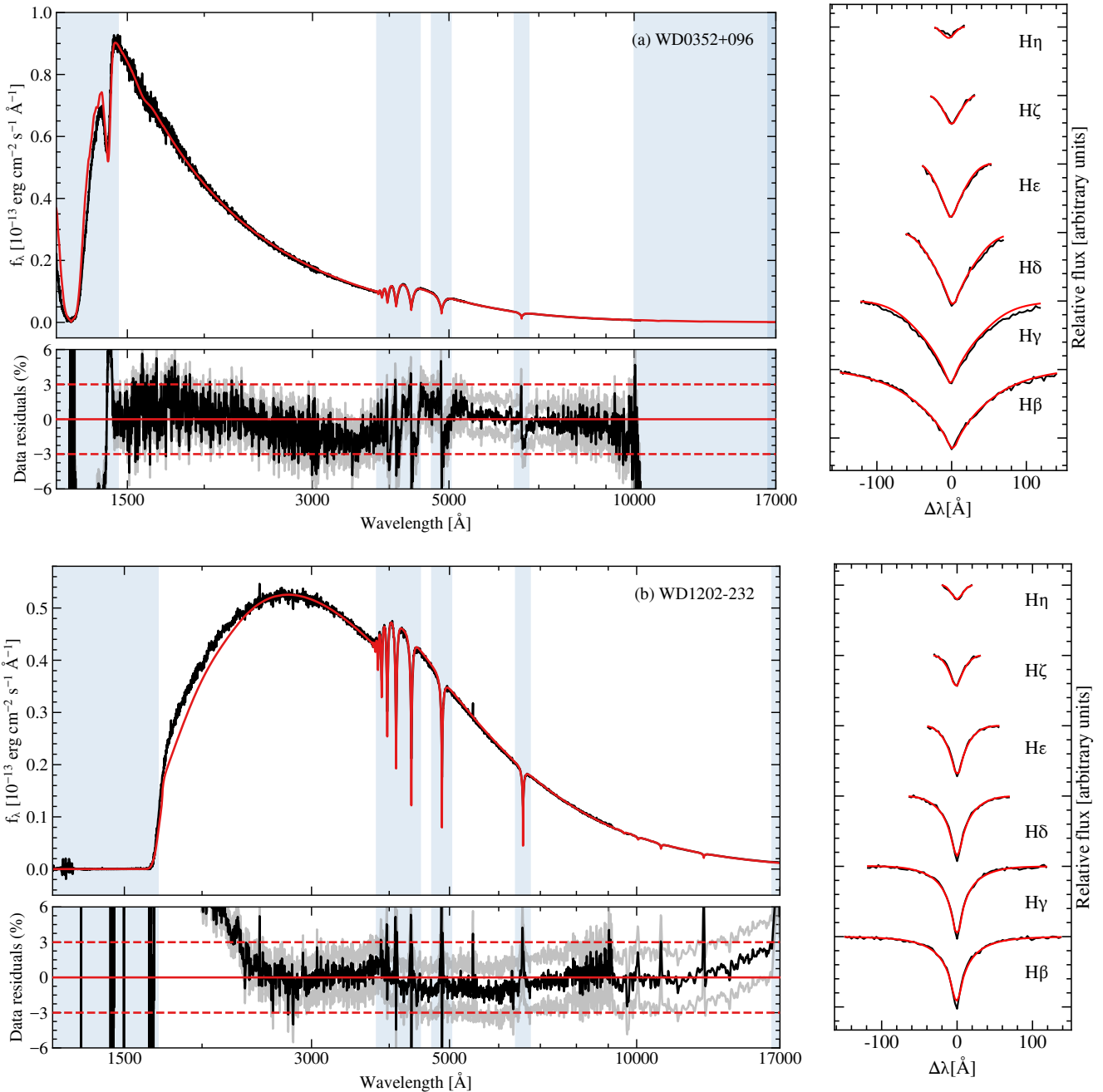


Figure 3. Similar to Figure 2 but for STIS and WFC3 spectrophotometry of the four extra white dwarfs proposed as flux standard candidates. (a) WD 0352+096 does not have WFC3 spectrophotometry.

4 DISCUSSION

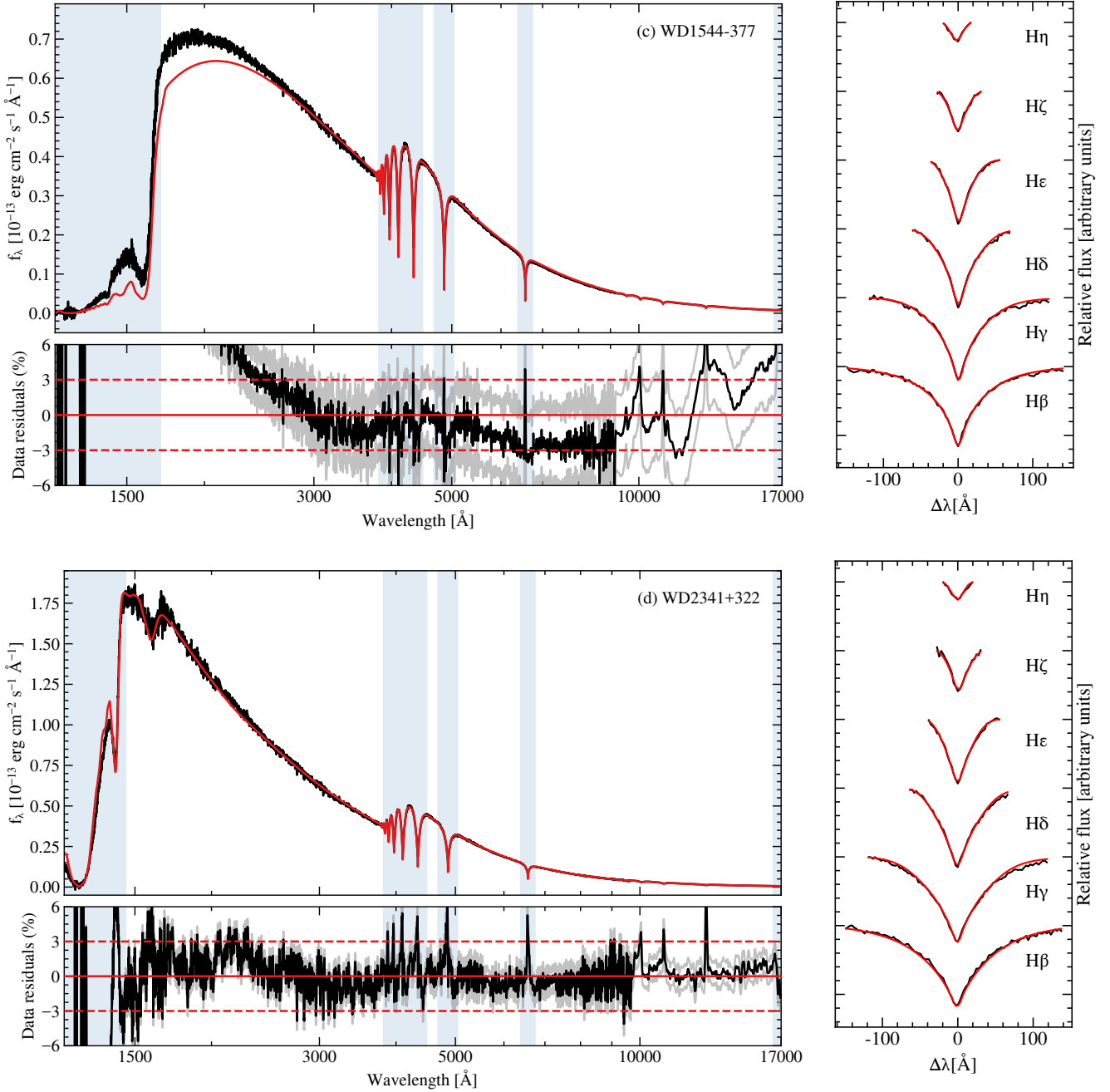
As the objective of this work is to fit the *HST* STIS and WFC3 spectrophotometry of 17 white dwarf flux standard candidates as accurately as possible, we tested different options in our fits to determine their implications.

For our Balmer line fits, we chose to fit from $H\beta$ to $H\eta$. The decision to omit $H\alpha$ was motivated from the fact that $H\alpha$ and the higher order Balmer lines are observed separately with two distinct STIS grating configurations. The G750L grating covers the range 5249 – 10 270 Å with a dispersion of 4.92 Å/pix, thus observes $H\alpha$, whereas the higher order Balmer lines are all observed using the

G430L grating which covers the range 2900 – 5700 Å with a dispersion of 2.73 Å/pix. The difference in dispersions shows the STIS sampling for $H\alpha$ is coarser than the other Balmer lines, with a lower resolution by a factor of ≈ 2 . Therefore including $H\alpha$ in the same fit as the higher order Balmer lines requires a well understood instrumental response, and uncertainties on that response may outweigh any additional constraints the extra Balmer line gives on the stellar parameters.

To obtain the most accurate results from Balmer line fits, models have to be convolved to the resolution of the instrument, i.e. the LSF, as this gives a true account of the light distribution along the primary

Figure 3 – continued



dispersion axis. Convolution with a Gaussian to a static resolution or full width half maximum (FWHM) is a valid approximation but using the instrumental resolution is the more accurate approach. STIS has four gratings which have slightly different instrumental profiles over their wavelength coverage. We selected the G430L grating LSF as that covered H β to H η (see Section 3.1.2 for details). The LSF function we created is accurate within < 1 per cent to the actual LSF however this small uncertainty will have propagated into the best-fitting Balmer line parameters shown in Table 2.

When using the DA M - R relation from Bédard et al. (2020) we used thick hydrogen layers with $q_{\text{H}} = M_{\text{H}}/M_{\text{WD}} = 10^{-4}$ as this is the standard procedure for DA white dwarfs based on theories of post-asymptotic-giant-branch (post-AGB) evolution and the maximum

hydrogen mass for residual nuclear burning (Iben & Tutukov 1984; Althaus et al. 2010). The other option is to use thin hydrogen layers with $q_{\text{H}} = 10^{-10}$, which is normally employed for helium-dominated atmosphere white dwarfs (DB, DC, DQ, DZ). However, using thick vs thin H-layers for DA and non-DA white dwarfs is not a strict rule - studies have shown evidence for thin H-layers in DA white dwarfs (Fontaine & Wesemael 1987, 1997; Miller Bertolami et al. 2017; Bond et al. 2017; Cunningham et al. 2020). For the 17 white dwarfs in this study, using thin H-layers altered the T_{eff} best-fitting parameters by < 50 K and < 0.03 dex, resulting in the SED and Balmer line results being slightly more discrepant. Therefore, we conclude that thick H-layers is the more accurate assumption for this white dwarf network.

Table 4. Observed and synthetic photometry in the *Gaia* G , G_{BP} and G_{RP} bands, 2MASS J , H and K_S bands, and WISE $W1$ and $W2$ bands. The first row for each object is the observed photometry and error, then the second row is the synthetic magnitude computed from our best-fitting STIS and WFC3 T_{eff} and $\log g$ parameters. Values in parentheses are 1σ errors in mmag. WD 2117+539 has no WISE data, WD 1544–377 has no 2MASS nor WISE data, and WD 1919+145 only has an upper limit for the 2MASS J magnitude, so those fields are filled with dashes.

Object	<i>Gaia</i>			2MASS			WISE	
	G [mag]	G_{BP} [mag]	G_{RP} [mag]	J [mag]	H [mag]	K_S [mag]	$W1$ [mag]	$W2$ [mag]
Hot primary standards								
GD 153	13.311(3)	13.151(3)	13.632(4)	14.012(25)	14.209(37)	14.308(62)	14.374(27)	14.506(52)
	13.288	13.118	13.616	14.048	14.162	14.271	14.353	14.393
GD 71	13.000(3)	12.853(3)	13.305(4)	13.728(25)	13.901(35)	14.115(65)	14.012(29)	14.103(51)
	12.979	12.820	13.287	13.701	13.810	13.921	14.005	14.052
Warm flux standard candidates								
WD 0148+467	12.496(3)	12.469(3)	12.588(4)	12.768(24)	12.826(32)	12.846(30)	12.906(24)	12.952(27)
	12.499	12.456	12.588	12.771	12.801	12.864	12.893	12.904
WD 0227+050	12.821(3)	12.745(3)	12.996(4)	13.282(26)	13.367(33)	13.425(36)	13.435(24)	13.468(33)
	12.827	12.737	13.003	13.276	13.336	13.416	13.466	13.485
WD 0809+177	13.429(3)	13.376(3)	13.552(4)	13.762(25)	13.841(36)	13.941(51)	13.970(26)	14.069(47)
	13.425	13.361	13.553	13.778	13.822	13.892	13.930	13.944
WD 1105–340	13.700(3)	13.686(3)	13.771(4)	13.954(28)	13.982(39)	14.054(66)	13.951(25)	13.898(37)
	13.661	13.624	13.739	13.913	13.939	14.001	14.029	14.040
WD 1105–048	13.091(3)	13.045(3)	13.214(4)	13.405(26)	13.445(30)	13.544(56)	13.570(25)	13.574(36)
	13.096	13.037	13.217	13.429	13.471	13.537	13.573	13.585
WD 1327–083	12.355(3)	12.323(3)	12.458(4)	12.621(37)	12.677(41)	12.736(48)	13.328(27)	13.165(29)
	12.351	12.303	12.452	12.644	12.679	12.743	12.774	12.785
WD 1713+695	13.328(3)	13.282(3)	13.450(4)	13.618(23)	13.720(29)	13.739(55)	13.811(24)	13.843(27)
	13.317	13.257	13.441	13.659	13.701	13.770	13.806	13.820
WD 1911+536	13.247(3)	13.189(3)	13.391(4)	13.616(29)	13.734(46)	13.824(47)	13.795(24)	13.885(29)
	13.251	13.179	13.395	13.642	13.690	13.766	13.810	13.826
WD 1919+145	13.019(3)	12.980(3)	13.126(4)	-	13.452(55)	13.546(66)	12.412(47)	12.546(80)
	13.016	12.964	13.122	13.326	13.362	13.429	13.463	13.476
WD 2039–682	13.339(3)	13.288(3)	13.469(4)	13.729(26)	13.806(39)	13.800(50)	13.879(26)	13.934(38)
	13.330	13.265	13.463	13.703	13.746	13.822	13.864	13.880
WD 2117+539	12.393(3)	12.355(3)	12.496(4)	12.681(21)	12.785(23)	12.85(38)	-	-
	12.361	12.306	12.475	12.680	12.719	12.785	12.819	12.831
WD 2126+734	12.887(3)	12.836(3)	12.989(5)	13.096(31)	13.164(38)	13.166(44)	13.075(23)	13.110(25)
	12.879	12.819	13.001	13.214	13.256	13.323	13.359	13.372
WD 2149+021	12.777(3)	12.713(3)	12.930(4)	13.203(24)	13.286(37)	13.397(37)	13.385(25)	13.379(32)
	12.783	12.706	12.936	13.185	13.238	13.313	13.357	13.373
Extra flux standard candidates								
WD 0352+096	14.548(3)	14.520(3)	14.635(4)	14.831(41)	14.866(59)	15.061(99)	14.938(35)	15.116(81)
	14.544	14.500	14.634	14.827	14.856	14.923	14.956	14.969
WD 1202–232	12.738(3)	12.843(3)	12.548(4)	12.402(24)	12.301(27)	12.342(26)	12.318(25)	12.343(24)
	12.725	12.814	12.542	12.435	12.331	12.357	12.366	12.368
WD 1544–377	13.001(3)	13.036(3)	12.931(4)	-	-	-	-	-
	12.993	13.028	12.917	12.944	12.907	12.951	12.965	12.973
WD 2341+322	12.967(3)	12.964(3)	13.007(4)	13.171(29)	13.195(37)	13.179(28)	13.243(25)	13.291(29)
	12.951	12.929	12.996	13.142	13.159	13.218	13.242	13.254

4.1 Observed vs model fluxes

Our 3D DA LTE models successfully predict the observed *HST* STIS and WFC3 spectrophotometry fluxes within 3 per cent over most of the range 1450 – 16 000 Å (Figures 2, B1 and 3). The standard deviation of the flux residuals from the entire SED fit, in addition to the fits of only the UV and combined optical+NIR regions, are shown in Table 3. The median standard deviation flux residual of the entire fit wavelength range is 1.34 per cent for the warm flux standard candidates, 3.25 per cent for the extra candidates, and 1.41 per cent for all 17 candidates.

The two coolest white dwarfs, WD 1202–232 and WD 1544–377, have slight discrepancies between the observed and model fluxes between $\approx 1700 - 2700$ Å, causing their residuals to be ≈ 4.5 per cent. There are known modelling uncertainties for cool white dwarfs ($T_{\text{eff}} \lesssim 10\,000$ K) in the near-UV, as the total opacity is affected by

the far red wing of the Lyman- α line where H and H₂ collisions significantly broaden the absorption line profile at those densities (Kowalski & Saumon 2006; Saumon et al. 2022). While potential issues with this opacity have been discussed in the context of UV and optical data of white dwarfs cooler than ≈ 6000 K (Saumon et al. 2014; Caron et al. 2023; O’Brien et al. 2024), we speculate that our precise STIS UV data may have uncovered a related, milder issue at warmer temperatures. If we fit the SEDs of the two coolest white dwarfs in the network starting at 2300 Å then the flux residuals reduce to 1.26 per cent for WD 1202–232 and 2.88 per cent for WD 1544–377. The observed WFC3 data for WD 1544–377 is slightly irregular (Figure 3c), with the issues likely caused by its wide binary companion (Section 4.4) contaminating the detected IR flux.

Fitting the UV and combined optical+NIR regions of the spectra separately yield median standard deviation flux residuals for the

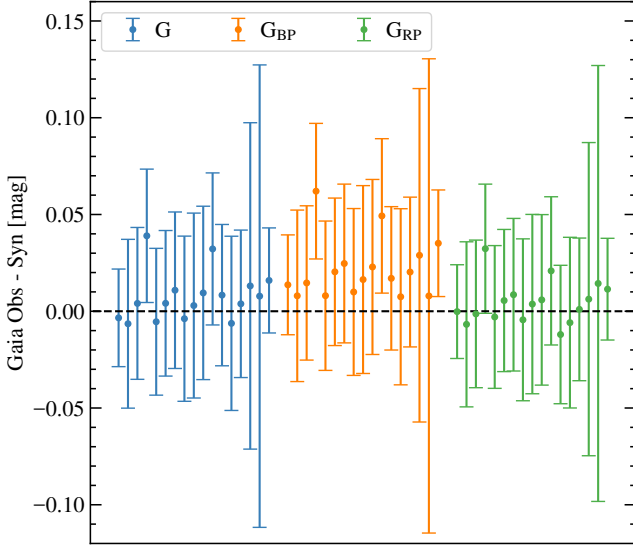


Figure 4. Observed minus synthetic photometry in the *Gaia* G , G_{BP} and G_{RP} bands. The x -axis coordinates within each band are uniformly spaced, ordered by RA with the warm flux standard candidates first, followed by the extra flux standard candidates. Observed (with errors) and synthetic magnitudes are given in Table 4. Error bars represent combined 1σ observed *Gaia* errors and synthetic magnitude errors, where synthetic errors are calculated from the T_{eff} and $\log g$ errors on our STIS and WFC3 SED fits (Table 2). The black dashed line indicates zero difference. Plot is based off fig. 10 in Axelrod et al. (2023).

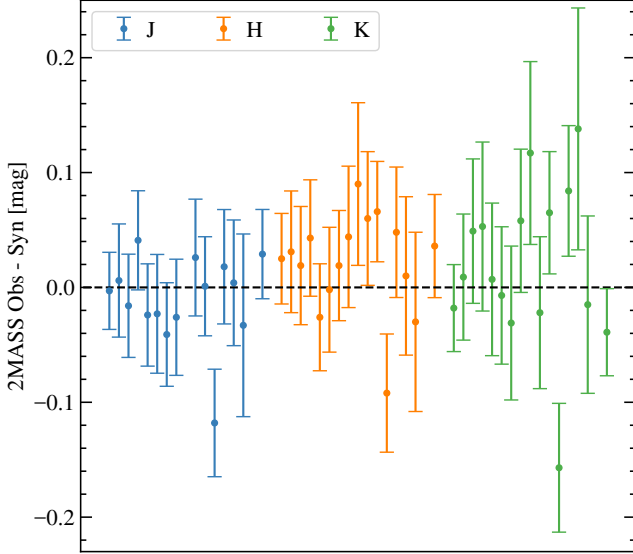


Figure 5. Same as Figure 4 but for 2MASS J , H and K_S bands. WD 1919+145 only has a J magnitude upper limit and WD 1544–377 has no observed 2MASS data so both white dwarfs are not included in this plot.

warm candidates of 1.43 per cent and 1.12 per cent, respectively, showing better agreement over the redder wavelengths. The same trend is seen when fitting only the four extra candidates (UV = 2.21 per cent and optical+NIR = 1.40 per cent), and all 17 candidates together (UV = 1.47 per cent and optical+NIR = 1.15 per cent). The proposed network of white dwarfs with $T_{\text{eff}} < 20\,000$ K can therefore

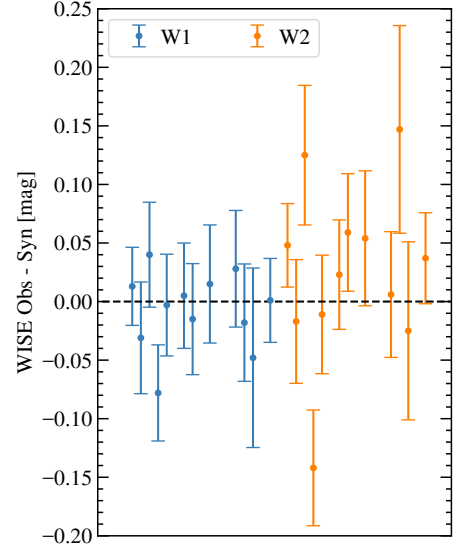


Figure 6. Same as Figure 4 but for WISE $W1$ and $W2$ bands. WD 2117+539 and WD 1544–377 have no observed WISE data so are not included in this plot. WD 1327–083, WD 1919+145 and WD 2126+734 are not included in this plot either because their observed and synthetic photometries are $> 3\sigma$ discrepant.

Table 5. Atmospheric parameters of the 17 DA white dwarfs proposed as flux standards from a photometric fit of the *Gaia* G , G_{BP} and G_{RP} bands. $\sigma_{T_{\text{eff}}}$ and $\sigma_{\log g}$ correspond to how many σ apart the best-fitting T_{eff} and $\log g$ parameters are from the *HST* STIS and WFC3 SED fit (Table 2) and *Gaia* photometric fit.

Object	T_{eff} [K]	$\log g$ [dex]	$\sigma_{T_{\text{eff}}}$	$\sigma_{\log g}$
Hot primary standards				
GD 153	35870 ± 1119	7.723 ± 0.031	3.531	2.553
GD 71	31526 ± 1092	7.760 ± 0.048	1.609	1.216
Warm flux standard candidates				
WD 0148+467	14110 ± 417	7.995 ± 0.037	0.834	0.760
WD 0227+050	18520 ± 583	7.858 ± 0.040	1.080	1.034
WD 0809+177	15790 ± 214	8.038 ± 0.017	2.071	1.761
WD 1105–340	13326 ± 420	8.079 ± 0.035	1.726	0.617
WD 1105–048	15469 ± 448	7.911 ± 0.036	0.743	0.741
WD 1327–083	15664 ± 444	7.919 ± 0.036	1.189	2.260
WD 1713+695	15495 ± 408	7.992 ± 0.032	1.277	0.961
WD 1911+536	16923 ± 468	8.283 ± 0.031	0.991	0.948
WD 1919+145	14979 ± 345	8.149 ± 0.025	1.002	0.791
WD 2039–682	16453 ± 390	8.467 ± 0.024	1.437	1.052
WD 2117+539	14679 ± 293	7.898 ± 0.026	2.656	1.690
WD 2126+734	15076 ± 83	7.893 ± 0.007	4.976	4.454
WD 2149+021	17187 ± 457	7.971 ± 0.034	1.015	0.994
Extra flux standard candidates				
WD 0352+096	14308 ± 355	8.291 ± 0.028	1.282	1.019
WD 1202–232	8655 ± 87	7.981 ± 0.025	1.505	1.256
WD 1544–377	10377 ± 33	8.021 ± 0.007	0.591	0.654
WD 2341+322	12358 ± 293	7.996 ± 0.031	1.517	0.927

accurately reproduce the CALSPEC flux scale in the optical+NIR regime to within 1.5 per cent.

We also fit the *HST* STIS and WFC3 spectrophotometry of the current hot standards GD 153 and GD 71, with our models successfully predicting the observed fluxes within 0.5 per cent over most of

the range 1450 – 16 000 Å. The standard deviation flux residuals are given in the first two rows of Table 3.

Our *HST* spectrophotometry consists of six separate observations from the four STIS gratings and two WFC3 gratings, which have been merged together. Small glitches in the SED can occur at the grating merge points (edges) causing residuals between observed and model fluxes to be > 3 per cent. Users of this white dwarf network as flux calibrators can remove these glitches if desired, but they have not been removed in this work.

Although we do not fit STIS spectra in the wavelength range 1140 – 1450 Å, discrepancies between model and observed SEDs can be found from a visual inspection of Figures 2 and B1. We note that the STIS flux calibration from the three primary hot white dwarf standards is uncertain at the ≈ 3 per cent level in this wavelength regime (see fig. 4 of Bohlin et al. 2020), a significant contrast to the sub-percent precision at longer wavelengths. This is largely attributed to differences in the predicted spectra from the TLUSTY and TMAP model atmosphere codes, and to a lesser degree on uncertainties in T_{eff} and $\log g$ determinations which propagate to model flux uncertainties. We note that Sahu et al. (2023) found a similar optical vs Lyman- α parameter discrepancy using *HST* Cosmic Origins Spectrograph (COS) observations of warm DA white dwarfs using instead the model atmospheres of (Koester 2010). Therefore these results could be an indication that *HST* primary flux calibration needs to be revisited in the UV. In the present work, additional uncertainties in this wavelength range may be related to missing physics in Lyman- α H_2^+ satellite opacities, in particular the treatment of electron broadening and N-body collisions (Allard & Kielkopf 2009; Gomez et al. 2024).

4.2 Atmospheric parameters

Independent T_{eff} and $\log g$ best-fitting parameters are obtained from fitting the *HST* STIS and WFC3 spectrophotometry SEDs and Balmer lines of the flux standard candidates. Statistical errors for both fitting routines are computed from the covariance matrix of the model atmosphere fit scaled by reduced χ^2 . However, using statistical errors alone do not account for all uncertainties in the fits thus are underestimates. We calculated the systematic error on T_{eff} and $\log g$ on SED fits as 1.1 per cent and 0.01 dex, respectively (Section 3.1.1), which gives more realistic uncertainties (Table 2).

It is more challenging to define a systematic uncertainty on Balmer line fits, with sensible options being to compare fits of the same star using different models or fit multiple observations or different lines from the same star with the same model. However, there is only one publicly available model for Stark line broadening (Tremblay & Bergeron 2009) and a limited number of Balmer lines to perform fitting. Reducing the number of lines in the fit drastically reduces precision and can introduce degeneracies between T_{eff} and $\log g$ (Tremblay & Bergeron 2009). Therefore we arbitrarily assign a scale factor of $\times 3$ on all Balmer line fit statistical errors, as this brings the Balmer line best-fitting T_{eff} to within 3σ of the SED best-fitting T_{eff} for 16/17 of the flux standard candidates (13/17 within 2σ and 8/17 within 1σ). This is a reasonable scale factor to account for uncertainties on Stark broadening profiles and non-ideal gas effects (Cho et al. 2022). The best-fitting $\log g$ parameters agree within 1σ for 16/17 flux candidates - applying the $\times 3$ scale factor to the $\log g$ uncertainties does not change this result. In this work we only quote the purely statistical uncertainties from Balmer line fitting and not the scaled-up values. However for the purpose of comparing results we suggest users multiply by three the values provided in Table 2. Overall the independent T_{eff} and $\log g$ best-fitting parameters from

our SED and Balmer line fits have a very tight linear correlation with no systematic deviations, and agree within 2.7 per cent in T_{eff} and 0.013 dex in $\log g$ as a median for the 17 flux standard candidates.

The SED and Balmer line best-fitting T_{eff} and $\log g$ parameters for the two hot primary standards, GD 153 and GD 71, agree within $\approx 1\sigma$ (Table 2). Compared to the parameters for these two standards in Table 1 of Bohlin et al. (2020), our SED parameters are within 1σ for GD 153 and within 1σ and 2σ for T_{eff} and $\log g$, respectively, for GD 71. Similarly, compared to the parameters in Table 2 of Narayan et al. (2019) our SED parameters are within 1σ and 2σ for T_{eff} and $\log g$, respectively, for GD 153, and within 1σ for GD 71. The strong agreement between best-fitting parameters in this work and the literature demonstrates the predictive power of the models adopted for our white dwarf flux candidate network.

4.3 Photometric analysis

The 17 white dwarfs proposed as flux standards in this work have optical photometry from *Gaia* G , G_{BP} and G_{RP} bands, in addition to IR photometry from 2MASS J , H and K_S bands and WISE $W1$ and $W2$ bands, with some exceptions. WD 2117+539 has no reported WISE data, potentially because it is near a bright star Gaia DR3 2176116584362421504 which could have contaminated the IR flux. WD 1544–377 has no 2MASS nor WISE data because it was likely not possible to accurately observe it due to its wide and bright binary companion (Section 4.4).

Our photometric analysis methods are detailed in Section 3.2 and the synthetic magnitudes computed are shown in Table 4, alongside observed magnitudes and uncertainties. The difference between observed and synthetic magnitudes for *Gaia*, 2MASS and WISE photometry are plotted in Figures 4 - 6 which illustrate the broad agreement across surveys and individual bands. For the *Gaia* photometric bands, there is 1σ agreement between observed and synthetic photometry for 16 of the white dwarfs in the G band, 14 white dwarfs in the G_{BP} band and all 17 white dwarfs in the G_{RP} band. All 17 white dwarfs agree within 2σ for the G and G_{BP} bands. The 16 white dwarfs with NIR 2MASS data all agree within 3σ across all bands, with 1σ agreement evident for 14, 12 and 10 white dwarfs across the J , H and K_S bands respectively. 15 white dwarfs in the network have IR WISE photometric data, of which 12 agree within 3σ with our synthetic magnitudes across both bands, 11 agree within 1σ in the $W1$ band and 7 agree within 1σ in the $W2$ band.

The WISE observed and synthetic photometries for WD 1327–083, WD 1919+145 and WD 2126+734 are between 6 – 16 σ discrepant. The reason for this discrepancy is likely due to contamination of the observed photometry. WD 1327–083 is in close proximity to a star; WD 2126+734 is in a crowded field and is in a WD+WD binary system (Section 4.4); and WD 1919+145 is in the Galactic plane with many nearby bright sources in the IR. Nevertheless, these stars are still suitable flux calibrators for spaced-based instruments or at moderate spatial resolution. The relatively high proper motions of our standards means their positions will vary with time and any of them could become temporarily blended with another star in the future.

Holberg & Bergeron (2006) made a similar residual comparison between observed and synthetic 2MASS J , H and K_S band photometries to that made in Figure 5, but for a larger sample of DA white dwarfs and without an upper T_{eff} constraint. The residual dispersions of $\lesssim 0.2$ mag across the bands measured in Holberg & Bergeron (2006) is similar to that calculated in this work.

In addition to synthetic photometry, we computed best-fitting atmospheric parameters from photometric fits of the *Gaia* G , G_{BP} and

G_{BP} observed photometry and parallaxes with our 3D LTE models (Section 3.2) which are displayed in Table 5. There is good agreement between our best-fitting photometric T_{eff} and $\log g$ parameters and SED parameters with 16 white dwarfs being within 3σ , 14 being within 2σ for T_{eff} and 15 being within 2σ for $\log g$. The photometric and SED parameters for WD 2126+734 are just over 3σ discrepant. We compared our photometric *Gaia* atmospheric parameters with those computed in Gentile Fusillo et al. (2021) and found all 17 objects from our network agree within 3σ .

The same photometric analysis on the hot standards GD 153 and GD 71 was performed, with the results shown in Tables 4 and 5. The observed and synthetic magnitudes for GD 153 agree within 1σ for all three bands in *Gaia* and 2MASS and the WISE W1 band, whereas there is a 2σ agreement for W2. For GD 71, the observed and synthetic magnitudes agree within 1σ for all three bands in *Gaia*, two bands in WISE and the 2MASS J band, whereas the 2MASS H and K_S bands agree within 2σ and 3σ , respectively. The best-fitting atmospheric parameters obtained from *Gaia* DR3 photometric fits agree with our STIS and WFC3 SED best-fitting parameters (Table 2) within 4σ and 3σ for T_{eff} and $\log g$, respectively, for GD 153, and within 2σ for GD 71.

A small systematic offset is apparent between observed and predicted *Gaia* G_{BP} magnitudes in Fig. 4, which suggests that *Gaia* and *HST* are not on the same relative or absolute flux scales (Maíz Apellániz & Weiler 2018). The offset is similar to that found in previous studies that have compared secondary *HST* flux standards with *Gaia* photometry (Narayan et al. 2019; Axelrod et al. 2023). Furthermore, the offset is consistent with a systematic difference in T_{eff} and mass found between Balmer line and photometric *Gaia* parameters for DA white dwarfs (Tremblay et al. 2019; Bergeron et al. 2019; Cukanovaite et al. 2021).

4.4 Flags on individual white dwarfs in our network

We searched the literature for our network of 17 white dwarfs to find any instances of metal detections/limits, variability, magnetic field detections/limits or binarity. The Transiting Exoplanet Survey Satellite (*TESS*; Ricker et al. 2014) Input Catalog (TIC) numbers are given for each white dwarf, so readers can check current *TESS* Sectors for variability when they are choosing calibrators.

Some white dwarfs are flagged with small metal abundances/limits or magnetic fields $\lesssim 150$ kG, but these would typically have a negligible effect on SEDs so are not removed from our network. One exception is the indirect effect of atmospheric metal pollution from planetary debris on the IR SED; while none of the white dwarfs in our network show a clear *WISE* excess attributable to a debris disk, metal polluted white dwarf calibrators are at greater risk of having so far undetected IR excess from debris. The white dwarfs in the El-Badry et al. (2021) *Gaia* eDR3 catalog of spatially resolved binary stars are flagged, with the projected separation in AU from their companion and the chance alignment ratio, which approximately represents the probability that a binary candidate is in a chance alignment. We present our findings below.

WD 0148+467 is not observed to vary in *TESS* (TIC 415880209).

WD 0227+050 is not observed to vary in *TESS* (TIC 422888592).

WD 0809+177 is not observed to vary in *TESS* (TIC 27634101).

WD 1105–340 has potentially contaminated *TESS* data (TIC 23226265). Landstreet & Bagnulo (2019) detected a probable dipolar magnetic field on the order of 150 kG and O’Brien et al. (2024) classified this star as DAH. Since it has $T_{\text{eff}} \approx 14\,000$ K and negligible convective energy transfer, the small magnetic field is not expected to significantly impact the atmospheric structure and predicted SED

(Tremblay et al. 2015b). We also note that the continuum and Balmer line fits are in good agreement despite possible Zeeman line splitting.

WD 1105–048 is not observed to vary in *TESS* (TIC 53211451). Valyavin et al. (2006) stated this star has a rotation period longer than 3 h. Aznar Cuadrado et al. (2004) discovered an average magnetic field of -2.1 kG with polarimetry data from the FOcal Reducer and low dispersion Spectrograph (FORs1; Appenzeller et al. 1998), where different field values from two observations were obtained, potentially indicating stellar rotation. Valyavin et al. (2006) found a variable longitudinal magnetic field from $\approx 0 - 8$ kG. Koester et al. (2009) found no detectable magnetic field nor peculiarities in UVES/VLT (Ultraviolet and Visual Echelle Spectrograph/Very Large Telescope) spectra obtained for the ESO SNe Ia Progenitor Survey (SPY). However, this star was flagged as a magnetic white dwarf in Bagnulo & Landstreet (2018) with FORs2 and the Intermediate-dispersion Spectrograph and Imaging System (ISIS) on the William Herschel Telescope (WHT), with a suspected variable weak field between $\langle B_z \rangle \approx 0 - 2.1$ kG and unknown period. This star has the spectral type DAH+dM in Bagnulo & Landstreet (2022) and DAH in O’Brien et al. (2024). At $T_{\text{eff}} \approx 15\,800$ K, it is too warm for magnetic fields to have an effect on atmospheric structure and predicted SED. WD 1105–048 is in a resolved WD+MS binary system with an M dwarf companion LP 672-2 (*Gaia* DR3 3788190605663811840) at a projected separation of 6944 AU and chance alignment of $1.08\text{E-}04$ (Oswalt et al. 1988; Aznar Cuadrado et al. 2004; Holberg et al. 2016; Toonen et al. 2017; El-Badry et al. 2021).

WD 1327–083 has no *TESS* data (TIC 422888592). Bagnulo & Landstreet (2018) observed this star once with ISIS and once with FORs2, measuring $\langle B_z \rangle = -0.9 \pm 0.4$ kG and $\langle B_z \rangle = -0.3 \pm 0.2$ kG, respectively. Given the non-significant detection, this white dwarf has the spectral type DA (Bagnulo & Landstreet 2021, 2022). This star is in a resolved WD+MS binary system with an M dwarf companion LHS 353 (*Gaia* DR3 3630015546177181952) at a projected separation of 8085 AU and chance alignment of $8.66\text{E-}09$ (Perryman et al. 1997; Farihi et al. 2005; Holberg et al. 2016; Toonen et al. 2017; El-Badry et al. 2021).

WD 1713+695 is not observed to vary in *TESS* (TIC 219863212).

WD 1911+536 is not observed to vary in *TESS* (TIC 298900716).

WD 1919+145 has potentially contaminated *TESS* data (TIC 338305380) due to it being in the Galactic plane. Zuckerman et al. (2003) state this star has $\log(\text{Ca}/\text{H}) < -8.838$ according to High Resolution Echelle Spectrometer (HIRES) echelle spectra from the Keck telescope.

WD 2039–682 is not observed to vary in *TESS* (TIC 372109346). Koester et al. (1998) identified a broadened $\text{H}\alpha$ core in this white dwarf, which could be explained by rotation or a magnetic field of ≈ 50 kG, although a distinction was not possible without circular polarization measurements. No magnetic field has been confirmed in the literature.

WD 2117+539 is not observed to vary in *TESS* (TIC 314771701).

WD 2126+734 is not observed to vary in *TESS* (TIC 323139945). This star is in a WD+WD binary system with WD 2126+734B (*Gaia* DR3 2274076301516712704) at a projected separation of 42 AU and chance alignment of $6.59\text{E-}08$ (Zuckerman et al. 1997; Farihi et al. 2005; Holberg et al. 2016; El-Badry et al. 2021; Heintz et al. 2024; O’Brien et al. 2024). Despite WD 2126+734 and its companion being physically close together, they have an angular separation of $1.74''$ because this is a very nearby white dwarf (22.2 pc; Table 1) so they are easily resolved by *HST*, *JWST* and *Gaia*. The observations made by 2MASS and WISE are likely blended due to these telescopes having resolutions $\gtrsim 4''$.

WD 2149+021 is not observed to vary in *TESS* (TIC 405122007).

A log (Ca/H) abundance between -8.0 and -7.6 has been measured in this white dwarf leading to it being classified as a DAZ in some literature (Koester et al. 2005; Koester & Wilken 2006; Berger et al. 2005; Kilic et al. 2006; Farihi et al. 2009; Kawka et al. 2011; O’Brien et al. 2024). While this small amount of metal pollution is not expected to impact the predicted SED which is dominated by hydrogen opacities at all continuum wavelengths according to our models, it has more risk of having a so far unseen debris disk.

WD 0352+096 is not observed to vary in *TESS* (TIC 415339071).

WD 1202–232 is not observed to vary in *TESS* (TIC 398243520). A log (Ca/H) abundance between -9.8 and -9.7 and log (Fe/H) abundance between -8.0 and -7.85 has been measured in this white dwarf leading to it being classified as a DAZ in some literature (Zuckerman et al. 2003; Koester et al. 2005; Koester & Wilken 2006; Farihi et al. 2009; Kawka et al. 2011; Kawka & Vennes 2012; Subasavage et al. 2017; Caron et al. 2023; O’Brien et al. 2024).

WD 1544–377 is not in *TESS*. Zuckerman et al. (2003) state this star has $\log(\text{Ca}/\text{H}) < -10.282$ according to HIRES echelle spectra from the Keck telescope. This white dwarf is in a WD+MS binary system with the high proper motion star HD 140901 (Gaia DR3 6009538585839374336) at a projected separation of 220 AU and angular separation of $14.6''$, with a chance alignment of $1.2\text{E-}05$ (Zuckerman et al. 2003; Holberg et al. 2016; El-Badry et al. 2021; O’Brien et al. 2024). The *Gaia* DR3 *G* magnitude of the companion is 5.834 mag. Note that the binary companion is incorrectly listed in Holberg et al. (2008).

WD 2341+322 is not observed to vary in *TESS* (TIC 288144896). Zuckerman et al. (2003) state this star has $\log(\text{Ca}/\text{H}) < -9.531$ according to HIRES echelle spectra from the Keck telescope. This white dwarf is not in the El-Badry et al. (2021) wide binary catalog nor is there any evidence of binarity in *Gaia*, but it is listed as a common proper motion companion in a non-interacting binary system in previous literature (McCook & Sion 1999; Zuckerman et al. 2003; Holberg et al. 2016).

4.5 White dwarfs as IR calibrators

White dwarfs are widely used for flux calibration in UV and optical regimes, along with A- and G-stars. The current three primary white dwarf standards achieve an accuracy better than 1 per cent at optical wavelengths and provide modelled SEDs which extend calibration from the UV to NIR (Bohlin et al. 2019, 2020). Using predicted SEDs from different model atmosphere codes, Bohlin et al. (2020) suggest that white dwarf flux calibration precision may be as good as 1 per cent up to $10\ \mu\text{m}$. Bohlin et al. (2011) and Gentile Fusillo et al. (2020) initially explored the accuracy of extending white dwarf flux calibration into the NIR and found modelled SEDs to be consistent with the *HST* flux scale within a few per cent. Recent work advancing *HST* primary calibration show promising agreement between the Sirius spectrum through the Spitzer Space Telescope Infrared Array Camera (IRAC) bands to $\approx 5\ \mu\text{m}$ (Bohlin et al. 2022; Rieke et al. 2023).

This work expands upon previous studies and proposes 17 white dwarfs with $T_{\text{eff}} < 20\,000\ \text{K}$ as IR calibrators. This network of white dwarfs is well-suited to provide an independent estimate for uniform calibration to the MIR as they have relatively featureless SEDs and lack variability. Also, IR opacities consists in well understood hydrogen free-free, bound-free and bound-bound transitions (Saumon et al. 2022), as shown by Figure 7 which is based on the same model atmospheres and spectra (Tremblay et al. 2013) as those used to fit our observed white dwarf network and predict their full SEDs. Considering this, and since the SEDs of these white dwarfs peak at UV,

optical and NIR wavelengths, we predict that these white dwarfs can be reliably used as flux standards for IR observations. This needs to be tested with *JWST* spectrophotometric observations, since *WISE* observations are limited in wavelength coverage and precision (≈ 5 per cent level). Such observations would also determine if any of our calibrators are inappropriate for the IR, such as from having debris disks or planets (Mullally et al. 2024).

The *JWST* absolute flux calibration programme is designed on *HST* absolute calibration therefore our network can provide another estimate for *JWST* calibration, set limits on the precision and provide legacy for its IR instruments (Gordon et al. 2022). We have shown that cool white dwarf stars are valuable NIR and potentially MIR calibrator additions and a composite approach to calibration with white dwarfs, A- and G-stars should be used to obtain the best possible results.

5 CONCLUSIONS

We have analysed *HST* STIS and WFC3 spectrophotometry of 17 DA white dwarfs with $T_{\text{eff}} < 20\,000\ \text{K}$ to investigate their reliability as flux calibrators, specifically in the IR regime. The stars in our network have significantly lower T_{eff} values than current hot DA primary standards (Bohlin et al. 2020), in addition to recent networks of hot but faint DA stars (Narayan et al. 2016, 2019; Axelrod et al. 2023), which has multiple advantages: their SEDs peak closer to the optical/NIR regime; have a larger sky density; NLTE effects and UV metal line blanketing have a negligible effect on continuum fluxes. Convection in cooler white dwarfs is not a significant issue either as our state-of-the-art 3D DA LTE model atmospheres account for convective effects without free parameters.

The results from this study show our model atmospheres successfully predict the observed fluxes of all 17 white dwarfs within 3 per cent over most of the wavelength range $1450 - 16\,000\ \text{\AA}$. The median standard deviation flux residual for all 17 candidates over the entire fit wavelength range is 1.41 per cent, with the coolest white dwarf residuals being ≈ 3 per cent. The residuals when fitting the UV and optical+NIR regions separately for the 17 candidates are 1.47 per cent and 1.15 per cent, respectively. Therefore, this network of white dwarfs cooler than current primary standards are fully consistent with the *HST*/CALSPEC flux scale over the UV, optical and NIR regimes.

Spectrophotometric fits of the observed *HST* STIS and WFC3 SEDs and Balmer lines of the 17 flux standard candidates yield independent atmospheric parameters. The best-fitting T_{eff} for 16 stars agree within 3σ and the best-fitting $\log g$ for all 17 stars agree within 2σ . Photometric fits of the observed *Gaia* DR3 *G*, *G_{BP}* and *G_{RP}* photometry results in 3σ agreement for all 17 stars with the best-fitting SED T_{eff} and $\log g$ parameters. Therefore we find excellent agreement between independent atmospheric parameters for our network.

We also computed synthetic magnitudes for *Gaia* *G*, *G_{BP}* and *G_{RP}* bands, 2MASS *J*, *H* and *K_S* bands and WISE *W1* and *W2* bands so we could compare them with observed photometry. All 17 white dwarfs in our network agree within 2σ for the three optical *Gaia* photometric bands. For the IR photometric bands in 2MASS and WISE, all the white dwarfs in our network with 2MASS data agree within 3σ and 12/15 with WISE data agree within 3σ .

To conclude, our network of 17 DA white dwarfs with $T_{\text{eff}} < 20\,000\ \text{K}$ represents a valuable addition to available flux standards. These stars provide reliable independent estimates for secondary IR SEDs and the legacy for current and future IR instruments onboard spacecraft such as the *JWST*, *Euclid* and *RST*, in addition to ground

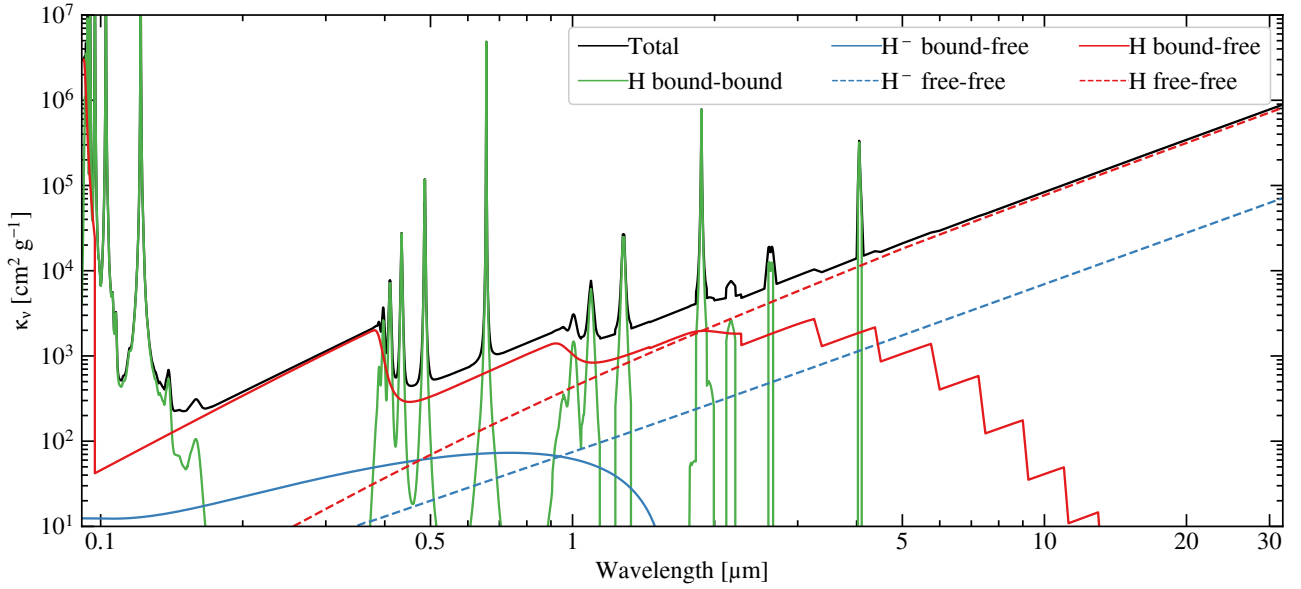


Figure 7. Dominant contributions to the radiative opacity of DA white dwarfs as a function of wavelength. The opacities shown are for a $T_{\text{eff}} = 12\,000\text{ K}$ white dwarf. A $\log g$ of 8.0 dex is assumed and the opacities are evaluated for the conditions at the photosphere. Based off the bottom panel of Fig. 17 in [Saumon et al. \(2022\)](#).

based observatories such as the ELT (e.g. MICADO). The synthetic spectra of our network are available with the electronic distribution of this article and on CALSPEC⁷. Observers can select the most suitable flux standards for calibrating their observations based on specific wavelength coverage and target requirements.

ACKNOWLEDGEMENTS

This research received funding from the European Research Council under the European Union’s Horizon 2020 research and innovation programme number 101002408 (MOS100PC). This research is based on observations made with the NASA/ESA *Hubble Space Telescope* obtained from the Space Telescope Science Institute, which is operated by the Association of Universities for Research in Astronomy, Inc., under NASA contract NAS 5–26555. Support for Program number (16249) was provided through a grant from the STScI under NASA contract NAS5- 26555. These observations are associated with programs GP-14213, GP-15485, GP-16249. This work has made use of data from the European Space Agency (ESA) mission *Gaia* (<https://www.cosmos.esa.int/gaia>), processed by the *Gaia* Data Processing and Analysis Consortium (DPAC, <https://www.cosmos.esa.int/web/gaia/dpac/consortium>). Funding for the DPAC has been provided by national institutions, in particular the institutions participating in the *Gaia* Multilateral Agreement. This publication makes use of data products from the Two Micron All Sky Survey, which is a joint project of the University of Massachusetts and the Infrared Processing and Analysis Center/California Institute of Technology, funded by the National Aeronautics and Space Administration and the National Science Foundation. This publication makes use of data products from the Wide-field Infrared Survey Explorer, which is a joint project of the University of California, Los Angeles, and the Jet Propulsion Labo-

ratory/California Institute of Technology, funded by the National Aeronautics and Space Administration.

DATA AVAILABILITY

All data underlying this paper are publicly available from the relevant survey archives. The model atmospheres used in this paper are available upon reasonable request of the author. The model SEDs for the network of 17 cooler white dwarf flux standards can be found in the electronic distribution of this article and on CALSPEC⁸ at <https://www.stsci.edu/hst/instrumentation/reference-data-for-calibration-and-tools/astronomical-catalogs/calspec>.

REFERENCES

- Allard N. F., Kielkopf J. F., 2009, *A&A*, **493**, 1155
 Althaus L. G., Córscico A. H., Bischoff-Kim A., Romero A. D., Renedo I., García-Berro E., Miller Bertolami M. M., 2010, *ApJ*, **717**, 897
 Appenzeller I., et al., 1998, *The Messenger*, **94**, 1
 Axelrod T., et al., 2023, *ApJ*, **951**, 78
 Aznar Cuadrado R., Jordan S., Napiwotzki R., Schmid H. M., Solanki S. K., Mathys G., 2004, *A&A*, **423**, 1081
 Bagnulo S., Landstreet J. D., 2018, *A&A*, **618**, A113
 Bagnulo S., Landstreet J. D., 2021, *MNRAS*, **507**, 5902
 Bagnulo S., Landstreet J. D., 2022, *ApJ*, **935**, L12
 Bédard A., Bergeron P., Brassard P., Fontaine G., 2020, *ApJ*, **901**, 93
 Berger L., Koester D., Napiwotzki R., Reid I. N., Zuckerman B., 2005, *A&A*, **444**, 565
 Bergeron P., Dufour P., Fontaine G., Coutu S., Blouin S., Genest-Beaulieu C., Bédard A., Rolland B., 2019, *ApJ*, **876**, 67
 Bohlin R. C., 2014, *AJ*, **147**, 127

⁷ The models for WD 1202–232 and WD 1544–377 are not included in CALSPEC due to potential modelling issues and/or contamination in the IR.

⁸ The models for WD 1202–232 and WD 1544–377 are not included in CALSPEC due to potential modelling issues and/or contamination in the IR.

- Bohlin R. C., et al., 2011, *AJ*, **141**, 173
- Bohlin R. C., Gordon K. D., Tremblay P. E., 2014, *PASP*, **126**, 711
- Bohlin R. C., Deustua S. E., de Rosa G., 2019, *AJ*, **158**, 211
- Bohlin R. C., Hubeny I., Rauch T., 2020, *AJ*, **160**, 21
- Bohlin R. C., Krick J. E., Gordon K. D., Hubeny I., 2022, *AJ*, **164**, 10
- Bond H. E., Bergeron P., Bédard A., 2017, *ApJ*, **848**, 16
- Brout D., et al., 2022, *ApJ*, **938**, 111
- Busso G., et al., 2022, Gaia DR3 documentation Chapter 5: Photometric data, Gaia DR3 documentation, European Space Agency; Gaia Data Processing and Analysis Consortium.
- Byrd R. H., Schnabel R. B., Shultz G. A., 1987, *SIAM Journal on Numerical Analysis*, **24**, 1152
- Calamida A., et al., 2022, *ApJ*, **940**, 19
- Caron A., Bergeron P., Blouin S., Leggett S. K., 2023, *MNRAS*, **519**, 4529
- Cho P. B., Gomez T. A., Montgomery M. H., Dunlap B. H., Fitz Axen M., Hobbs B., Hubeny I., Winget D. E., 2022, *ApJ*, **927**, 70
- Cukanovaite E., Tremblay P.-E., Bergeron P., Freytag B., Ludwig H.-G., Steffen M., 2021, *MNRAS*, **501**, 5274
- Cunningham T., Tremblay P.-E., Gentile Fusillo N. P., Hollands M., Cukanovaite E., 2020, *MNRAS*, **492**, 3540
- El-Badry K., Rix H.-W., Heintz T. M., 2021, *MNRAS*, **506**, 2269
- Farihi J., Becklin E. E., Zuckerman B., 2005, *ApJS*, **161**, 394
- Farihi J., Jura M., Zuckerman B., 2009, *ApJ*, **694**, 805
- Fitzpatrick E. L., Massa D., 1999, *ApJ*, **525**, 1011
- Fontaine G., Wesemael F., 1987, in Philip A. G. D., Hayes D. S., Liebert J. W., eds, IAU Colloq. 95: Second Conference on Faint Blue Stars. pp 319–326
- Fontaine G., Wesemael F., 1997, in Isern J., Hernanz M., Garcia-Berro E., eds, *Astrophysics and Space Science Library* Vol. 214, White dwarfs. p. 173, doi:10.1007/978-94-011-5542-7_26
- Gaia Collaboration et al., 2023, *A&A*, **674**, A1
- Gentile Fusillo N. P., Tremblay P.-E., Bohlin R. C., Deustua S. E., Kalirai J. S., 2020, *MNRAS*, **491**, 3613
- Gentile Fusillo N. P., et al., 2021, *MNRAS*, **508**, 3877
- Gianninas A., Bergeron P., Dupuis J., Ruiz M. T., 2010, *ApJ*, **720**, 581
- Gomez T. A., Stambulchik E., White J., 2024, *Phys. Rev. A*, **109**, 052804
- Gordon K. D., et al., 2022, *AJ*, **163**, 267
- Gordon K. D., Clayton G. C., Declerik M., Fitzpatrick E. L., Massa D., Misselt K. A., Tollerud E. J., 2023, *ApJ*, **950**, 86
- Greenstein J. L., Oke J. B., 1979, *ApJ*, **229**, L141
- Heintz T. M., Hermes J. J., Tremblay P. E., Ould Rouis L. B., Reding J. S., Kaiser B. C., van Saders J. L., 2024, *ApJ*, **969**, 68
- Holberg J. B., Bergeron P., 2006, *AJ*, **132**, 1221
- Holberg J. B., Wesemael F., Wegner G., Bruhweiler F. C., 1985, *ApJ*, **293**, 294
- Holberg J. B., Sion E. M., Oswald T., McCook G. P., Foran S., Subasavage J. P., 2008, *AJ*, **135**, 1225
- Holberg J. B., Oswald T. D., Sion E. M., McCook G. P., 2016, *MNRAS*, **462**, 2295
- Hounsell R., et al., 2018, *ApJ*, **867**, 23
- Iben I. J., Tutukov A. V., 1984, *ApJS*, **54**, 335
- Johnson H. L., 1965, *ApJ*, **141**, 923
- Kawka A., Vennes S., 2012, *MNRAS*, **425**, 1394
- Kawka A., Vennes S., Dinnbier F., Cibulková H., Németh P., 2011, in Schuh S., Drechsel H., Heber U., eds, *American Institute of Physics Conference Series* Vol. 1331, Planetary Systems Beyond the Main Sequence. AIP, pp 238–245 (arXiv:1012.2639), doi:10.1063/1.3556206
- Kilic M., von Hippel T., Leggett S. K., Winget D. E., 2006, *ApJ*, **646**, 474
- Koester D., 2010, *Mem. Soc. Astron. Italiana*, **81**, 921
- Koester D., Wilken D., 2006, *A&A*, **453**, 1051
- Koester D., Weidemann V., Zeidler-K. T. E. M., Vauclair G., 1985, *A&A*, **142**, L5
- Koester D., Dreizler S., Weidemann V., Allard N. F., 1998, *A&A*, **338**, 612
- Koester D., Rollenhagen K., Napiwotzki R., Voss B., Christlieb N., Homeier D., Reimers D., 2005, *A&A*, **432**, 1025
- Koester D., Voss B., Napiwotzki R., Christlieb N., Homeier D., Lisker T., Reimers D., Heber U., 2009, *A&A*, **505**, 441
- Kowalski P. M., Saumon D., 2006, *ApJ*, **651**, L137
- Landstreet J. D., Bagnulo S., 2019, *A&A*, **623**, A46
- Maíz Apellániz J., Weiler M., 2018, *A&A*, **619**, A180
- McCook G. P., Sion E. M., 1999, *ApJS*, **121**, 1
- Megessier C., 1995, *A&A*, **296**, 771
- Miller Bertolami M. M., Althaus L. G., Córscico A. H., 2017, in Tremblay P. E., Gaensicke B., Marsh T., eds, *Astronomical Society of the Pacific Conference Series* Vol. 509, 20th European White Dwarf Workshop. p. 435 (arXiv:1609.08683), doi:10.48550/arXiv.1609.08683
- Mullally S. E., et al., 2024, *ApJ*, **962**, L32
- Munday J., et al., 2024, *MNRAS*, **532**, 2534
- Napiwotzki R., et al., 2020, *A&A*, **638**, A131
- Narayan G., et al., 2016, *ApJ*, **822**, 67
- Narayan G., et al., 2019, *ApJS*, **241**, 20
- Nelan E. P., Wegner G., 1985, *ApJ*, **289**, L31
- O'Brien M. W., et al., 2024, *MNRAS*, **527**, 8687
- Oswalt T. D., Hintzen P. M., Luyten W. J., 1988, *ApJS*, **66**, 391
- Perryman M. A. C., et al., 1997, *A&A*, **323**, L49
- Rauch T., Werner K., Bohlin R., Kruk J. W., 2013, *A&A*, **560**, A106
- Ricker G. R., et al., 2014, in Oschmann Jacobus M. J., Clampin M., Fazio G. G., MacEwen H. A., eds, *Society of Photo-Optical Instrumentation Engineers (SPIE) Conference Series* Vol. 9143, Space Telescopes and Instrumentation 2014: Optical, Infrared, and Millimeter Wave. p. 914320 (arXiv:1406.0151), doi:10.1117/12.2063489
- Rieke G. H., Engelke C., Su K., Casagrande L., 2023, *AJ*, **165**, 99
- Rodrigo C., Solano E., Bayo A., 2012, SVO Filter Profile Service Version 1.0, IVOA Working Draft 15 October 2012, doi:10.5479/ADS/bib/2012ivoa.rept.1015R
- Sahu S., et al., 2023, *MNRAS*, **526**, 5800
- Saumon D., Holberg J. B., Kowalski P. M., 2014, *ApJ*, **790**, 50
- Saumon D., Blouin S., Tremblay P.-E., 2022, *Phys. Rep.*, **988**, 1
- Schultz G. V., Wiemer W., 1975, *A&A*, **43**, 133
- Scolnic D., et al., 2015, *ApJ*, **815**, 117
- Scolnic D., et al., 2022, *ApJ*, **938**, 113
- Skrutskie M. F., et al., 2006, *AJ*, **131**, 1163
- Stubbs C. W., Brown Y. J., 2015, *Modern Physics Letters A*, **30**, 1530030
- Subasavage J. P., et al., 2017, *AJ*, **154**, 32
- Tayar J., Claytor Z. R., Huber D., van Saders J., 2022, *ApJ*, **927**, 31
- Toonen S., Hollands M., Gänsicke B. T., Boekholt T., 2017, *A&A*, **602**, A16
- Tremblay P. E., Bergeron P., 2009, *ApJ*, **696**, 1755
- Tremblay P. E., Bergeron P., Gianninas A., 2011, *ApJ*, **730**, 128
- Tremblay P. E., Ludwig H. G., Steffen M., Freytag B., 2013, *A&A*, **559**, A104
- Tremblay P. E., Gianninas A., Kilic M., Ludwig H. G., Steffen M., Freytag B., Hermes J. J., 2015a, *ApJ*, **809**, 148
- Tremblay P. E., Fontaine G., Freytag B., Steiner O., Ludwig H. G., Steffen M., Wedemeyer S., Brassard P., 2015b, *ApJ*, **812**, 19
- Tremblay P. E., et al., 2017, *MNRAS*, **465**, 2849
- Tremblay P. E., Cukanovaite E., Gentile Fusillo N. P., Cunningham T., Hollands M. A., 2019, *MNRAS*, **482**, 5222
- Valyavin G., Bagnulo S., Fabrika S., Reisenegger A., Wade G. A., Han I., Monin D., 2006, *ApJ*, **648**, 559
- Wegner G., 1982, *ApJ*, **261**, L87
- Werner K., 1996, *ApJ*, **457**, L39
- Whittet D. C. B., van Breda I. G., 1980, *MNRAS*, **192**, 467
- Wilson R. F., et al., 2023, *ApJS*, **269**, 5
- Wright E. L., et al., 2010, *AJ*, **140**, 1868
- Xu S., Jura M., Koester D., Klein B., Zuckerman B., 2013, *ApJ*, **766**, L18
- Zuckerman B., Becklin E. E., Macintosh B. A., Bida T., 1997, *AJ*, **113**, 764
- Zuckerman B., Koester D., Reid I. N., Hüensch M., 2003, *ApJ*, **596**, 477

APPENDIX A: *HST* OBSERVATION LOG

APPENDIX B: SPECTROPHOTOMETRIC FITS FOR 11/13 WARM WHITE DWARFS

This paper has been typeset from a \LaTeX file prepared by the author.

Table A1. Log of *HST* STIS and WFC3 spectrophotometric observations for the 17 DA white dwarfs proposed as flux standards. The exposure time (t_{exp}), number of exposures (n_{exp}) and the duration of the observing run is given. Where observations were taken over multiple dates with multiple exposure times, numbers are separated by a forward slash (/).

Object	Telescope/Instrument	Date [yyyy-mm-dd]	Grating	t_{exp} [s]	n_{exp}	Duration [s]
Warm flux standard candidates						
WD 0148+467	HST/STIS	2021-08-07	G140L	1355.0	1	1355.0
		2021-08-07	G230L	718.0	1	718.0
		2021-08-07	G430L	410.0	1	410.0
		2021-08-07	G750L	2000.0	1	2000.0
	HST/WFC3	2021-07-30	G102	138.4	3	415.1
		2021-07-30	G141	115.5	3	346.4
WD 0227+050	HST/STIS	2021-12-19	G140L	953.0	1	953.0
		2021-12-19	G230L	980.0	1	980.0
		2021-12-19	G430L	306.0	1	306.0
		2021-12-19	G750L	1920.0	1	1920.0
	HST/WFC3	2021-09-22	G102	253.0	3	759.0
		2021-07-30	G141	207.1	3	621.4
WD 0809+177	HST/STIS	2022-02-21	G140L	1074.0	1	1074.0
		2022-02-21	G230L	870.0	1	870.0
		2022-02-21	G430L	300.0	1	300.0
		2022-02-21	G750L	1980.0	1	1980.0
	HST/WFC3	2021-09-18	G102	432.1	3	1296.4
		2021-09-18	G141	336.3	3	1008.9
WD 1105–340	HST/STIS	2022-01-27	G140L	1368.0	1	1368.0
		2022-01-27	G230L	600.0	1	600.0
		2022-01-27	G430L	324.0	1	324.0
		2022-01-27	G750L	1980.0	1	1980.0
	HST/WFC3	2021-08-03	G102	432.1	3	1296.4
		2021-08-03	G141	384.2	3	1152.7
WD 1105–048	HST/STIS	2022-04-02	G140L	1143.0	1	1143.0
		2022-04-02	G230L	780.0	1	780.0
		2022-04-02	G430L	340.0	1	340.0
		2022-04-02	G750L	1928.0	1	1928.0
	HST/WFC3	2021-12-15	G102	275.9	3	827.7
		2021-12-15	G141	230.1	3	690.2
WD 1327–083	HST/STIS	2016-04-15	G140L	1244.0	1	1244.0
		2016-04-15	G230L	605.0	1	605.0
		2016-04-15	G430L	200.0	1	200.0
		2016-04-15	G750L	936.0	1	936.0
	HST/WFC3	2016-04-15	G102	83.5	1	83.5
		2016-04-15	G141	60.1	3	60.1
WD 1713+695	HST/STIS	2022-07-07	G140L	1364.0	1	1364.0
		2022-07-07	G230L	910.0	1	910.0
		2022-07-07	G430L	342.0	1	342.0
		2022-08-29	G750L	2475.0	1	2475.0
	HST/WFC3	2021-09-20	G102	321.8	3	965.3
		2021-09-20	G141	275.9	3	827.7
WD 1911+536	HST/STIS	2021-10-01	G140L	1112.0	1	1112.0
		2021-10-01	G230L	1000.0	1	1000.0
		2021-10-01	G430L	330.0	1	330.0
		2021-10-01	G750L	2080.0	1	2080.0
	HST/WFC3	2021-07-24	G102	336.3	3	1008.9
		2021-07-24	G141	298.8	3	896.5
WD 1919+145	HST/STIS	2022-08-23	G140L	1237.0	1	1237.0
		2022-08-23	G230L	700.0	1	700.0
		2021/2022-10/08-06/23	G430L	330.0	2	660.0
		2022-08-23	G750L	1944.0	2	1944.0
	HST/WFC3	2021-07/09-21/14	G102	253.0	6	1517.9
		2021-07/09-21/14	G141	207.1	6	1242.9
WD 2039–682	HST/STIS	2022-08-01	G140L	1220.0	1	1220.0
		2022-08-01	G230L	1054.0	1	1054.0
		2022-08-01	G430L	342.0	1	342.0
		2022-08-01	G750L	2225.0	1	2225.0
	HST/WFC3	2021-07-27	G102	336.3	3	1008.9
		2021-07-27	G141	298.8	3	896.5

Table A1 – *continued*

Object	Telescope/Instrument	Date [yyyy-mm-dd]	Grating	t_{exp} [s]	n_{exp}	Duration [s]
WD 2117+539	HST/STIS	2022-08-27	G140L	1437.0	1	1437.0
		2022-08-27	G230L	700.0	1	700.0
		2022-08-27	G430L	354.0	1	354.0
		2022-08-27	G750L	2060.0	1	2060.0
	HST/WFC3	2021-07/09-31/15	G102	230.1	6	1380.4
		2021-07/09-31/15	G141	184.2	6	1105.3
WD 2126+734	HST/STIS	2021-10-02	G140L	1400.0	1	1400.0
		2021-10-02	G230L	913.0	1	913.0
		2021-10-02	G430L	406.0	1	406.0
		2021-10-02	G750L	2200.0	1	2200.0
	HST/WFC3	2021-08-03	G102	253.0	3	759.0
		2021-08-03	G141	207.1	3	621.4
WD 2149+021	HST/STIS	2021-10-02	G140L	965.0	1	965.0
		2021-10-02	G230L	965.0	1	965.0
		2021-10-02	G430L	302.0	1	302.0
		2021-10-02	G750L	1920.0	1	1920.0
	HST/WFC3	2021-07-26	G102	207.1	3	621.4
		2021-07-26	G141	161.3/184.2	3	506.8
Extra flux standard candidates						
WD 0352+096	HST/STIS	2019-02-09	G140L	2379.0	1	2379.0
		2019-02-09	G230L	1101.0	1	1101.0
		2019-02-09	G430L	1200.0	1	1200.0
		1998-02/03-19	G750L	1980.0	2	3960.0
WD 1202–232	HST/STIS	2021-08-05	G140L	749.0/761.0	2	1510.0
		2016-06-15	G230L	2302.2	1	2302.2
		2021-08-05	G430L	1200.0	1	1200.0
		2021-08-05	G750L	1600.0	1	1600.0
	HST/WFC3	2021-07-25	G102	138.4	3	415.1
		2021-07-25	G141	88.0	3	264.0
WD 1544–377	HST/STIS	2021-10-03	G140L	1047.0	1	1047.0
		2021-10-03	G230L	1790.0	1	1790.0
		2021-10-03	G430L	300.0	1	300.0
		2021-10-03	G750L	1401.0	1	1401.0
	HST/WFC3	2021-07/09-29/27	G102	161.3/177.9	3/3	1017.7
		2021-07/09-29/27	G141	115.2/127.9	3/3	730.2
WD 2341+322	HST/STIS	2016-05-27	G140L	1370.0	1	1370.0
		2016-05-27	G230L	650.0	1	650.0
		2016-05-27	G430L	240.0	1	240.0
		2016-05-27	G750L	939.0	1	939.0
	HST/WFC3	2016-05-27	G102	176.0	1	176.0
		2016-05-27	G141	128.5	1	128.5

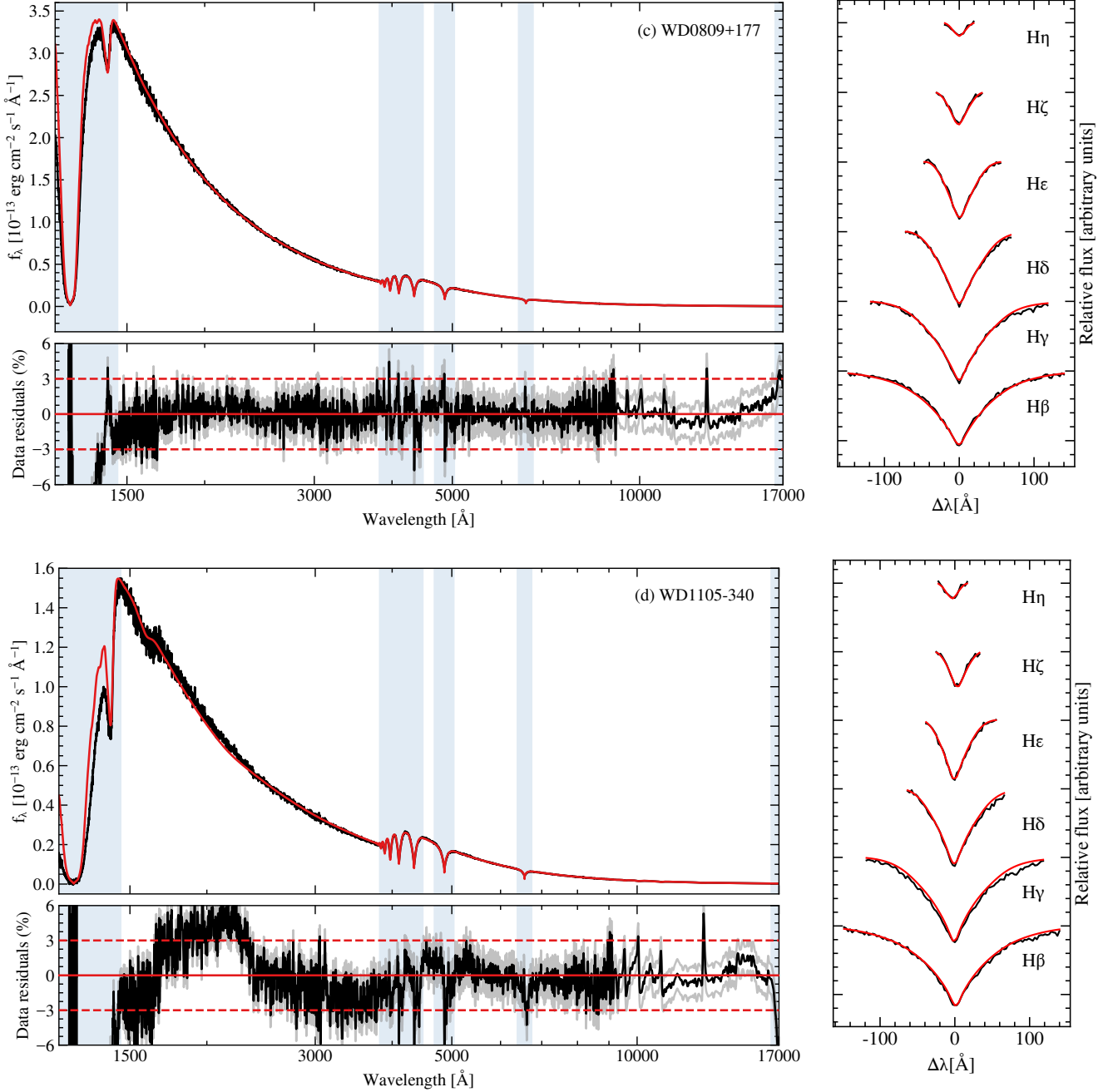


Figure B1. Spectrophotometric fits of the STIS and WFC3 data for 11/13 warm white dwarfs proposed as flux standard candidates, with the WD name of each star given in the corner of the top left panels. *Top left:* SED fit between the observed spectrophotometry (black) and best-fitting model (red). *Bottom left:* Flux residuals from the corresponding SED fit, where the black line is the calculated residual, grey lines indicate residuals $\pm 1\sigma$ using only the statistical errors from the fits, and red lines indicate 0 and ± 3 per cent flux residuals as a guide. The shaded blue regions in the left panels indicate wavelength ranges excluded from the fits. *Right:* Balmer line fits for $H\beta$ to $H\eta$ between the observed spectrophotometry (black) and best-fitting model (red). The line profiles are vertically offset for clarity. The best-fitting parameters for the SED and Balmer line fits are found in Table 2.

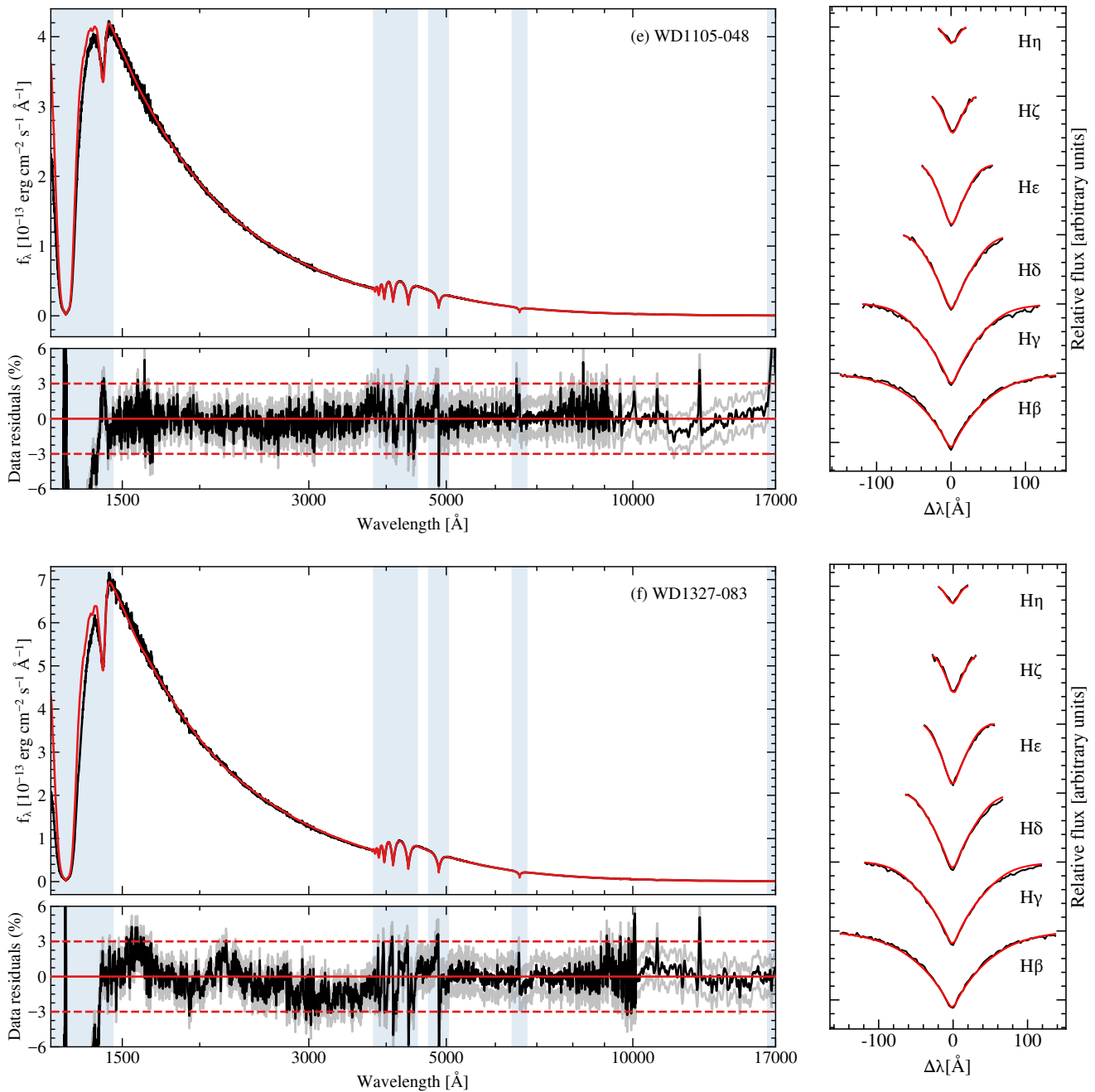
Figure B1 – *continued*

Figure B1 – continued

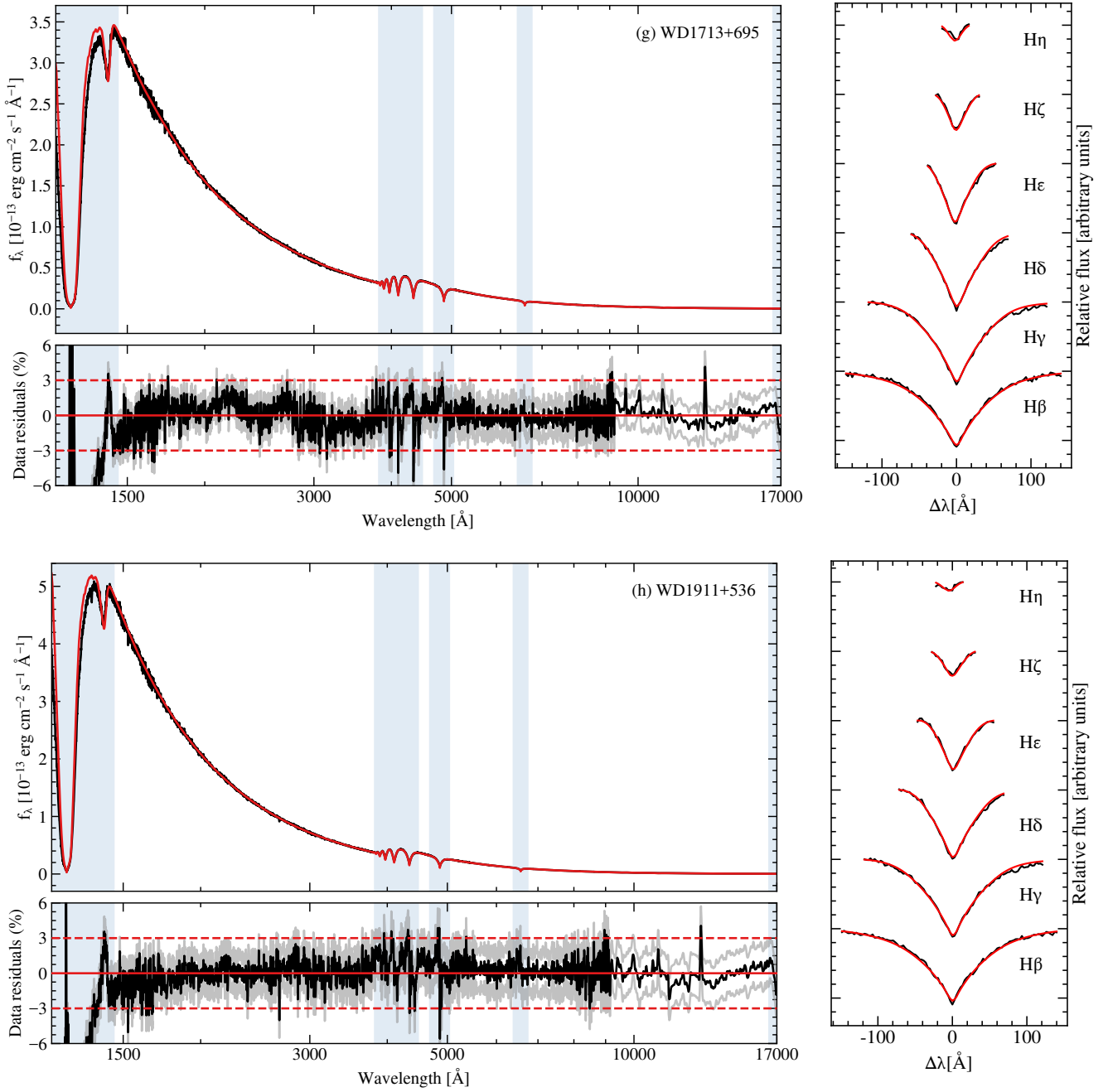


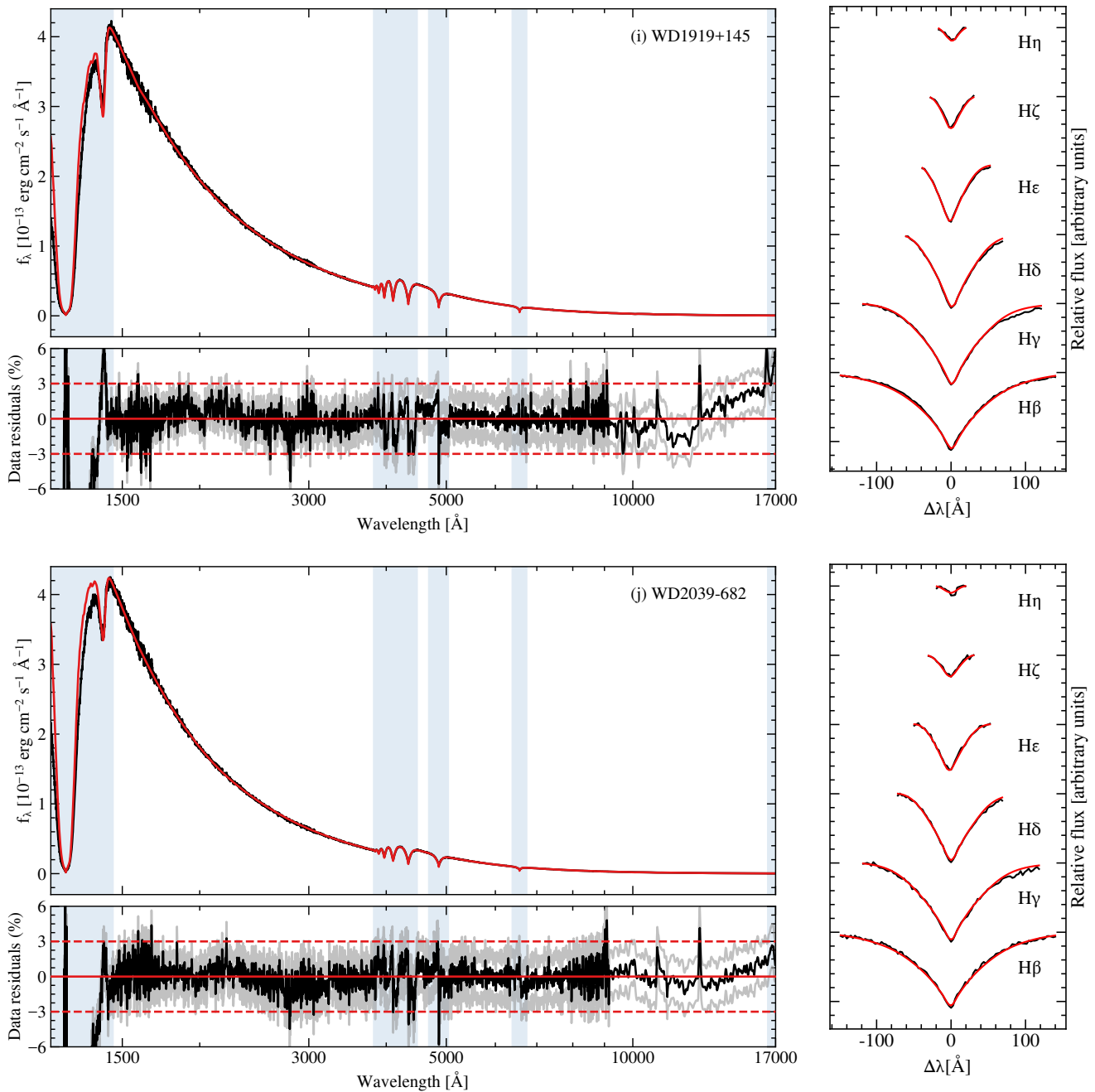
Figure B1 – *continued*

Figure B1 – continued

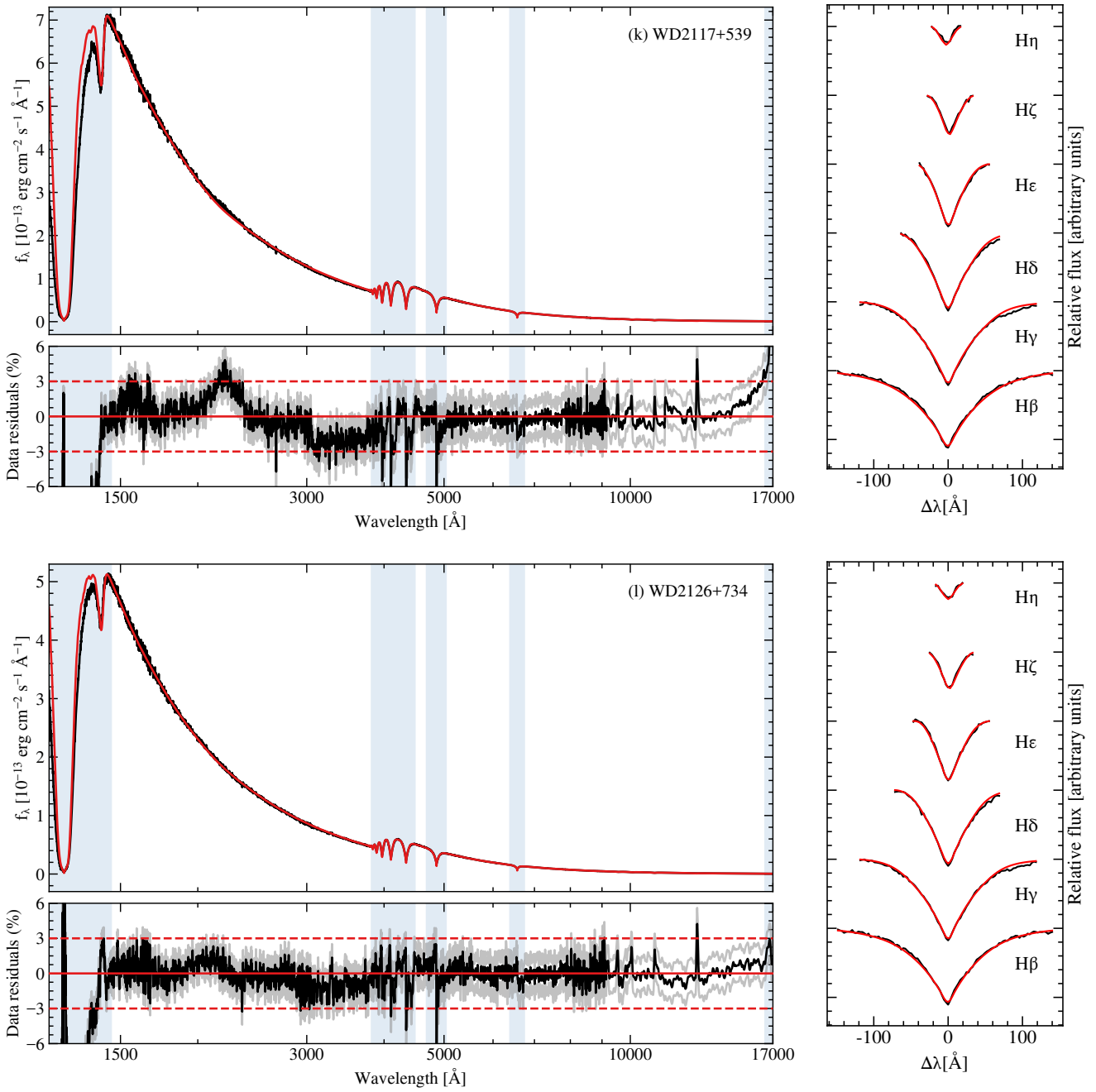


Figure B1 – *continued*